Ambiguity-resolved short-baseline positioning performance of LEO frequency-varying carrier phase signals

a feasibility study

Yang, S.; Khodabandeh, A.; Zaminpardaz, S.; Teunissen, P. J.G.

DOI
10.1007/s00190-025-01942-w

Publication date
2025

Document Version
Final published version

Published in
Journal of Geodesy

Journal of Geodesy (2025) 99:17
https://doi.org/10.1007/s00190-025-01942-w

ORIGINAL ARTICLE

Ambiguity-resolved short-baseline positioning performance of LEO frequency-varying carrier phase signals: a feasibility study

S. Yang[1] · A. Khodabandeh[1] · S. Zaminpardaz[2] · P. J. G. Teunissen[1,3]

Received: 4 December 2024 / Accepted: 28 January 2025

Abstract
While integer ambiguity resolution (IAR) enables GNSS to achieve real-time sub-centimeter-level positioning in open-sky environments, it can be easily hindered if the involved receivers are situated in areas with limited satellite visibility, such as in dense city environments. In such GNSS-challenged cases, commercial Low Earth Orbit (LEO) communication satellites can potentially augment GNSS by providing additional measurements. However, LEO satellites often lack code measurements, mainly transmitting satellite-specific frequency-varying carrier phase signals. This contribution aims to study the ambiguity-resolved baseline positioning performance of such phase-only signals, addressing the extent to which LEO constellations can realize near real-time positioning in standalone and GNSS-combined modes. Through a simulation platform, we analyze the distinct response of each LEO constellation (Iridium, Globalstar, Starlink, OneWeb, and Orbcomm) to IAR under various circumstances. Although achieving *single-receiver* high-precision positioning can be challenged by inaccuracies in the LEO satellite orbit products, the relative distance between two receivers can help overcome this limitation. As a result, centimeter-level relative positioning over short baselines can be made possible, even with a satellite elevation cut-off angle of 50 degrees, making it suitable for GNSS-challenged environments. This can be achieved with high-grade receiver clocks over very short baselines (∼5 km) and access to decimeter-level orbit products.

Keywords Global navigation satellite systems (GNSS) · Low earth orbit (LEO) communication satellites · Frequency-varying carrier phase signals · Integer ambiguity resolution (IAR)

1 Introduction

The ultra-precise carrier phase measurements of Global Navigation Satellite Systems (GNSS) can realize near real-time sub-centimeter level positioning when collected by terrestrial receivers tracking multiple GNSS satellites in open-sky environments (Leick et al. 2015). However, such precision can be easily compromised if receivers are located in urban canyons with limited visible satellites. Therefore, GNSS should be augmented with supporting sensory data so as to ensure the provision of reliable positioning, navigation and timing (PNT) services. In recent years, thousands of commercial Low Earth Orbit (LEO) communication satellites from multiple constellations, including Iridium, Orbcomm, Globalstar, OneWeb, and Starlink, have been deployed by distinct broadband internet providers (Dietrich et al. 1998; Ilcev 2005; Reid et al. 2018; Khalife and Kassas 2019). Considering that these LEO satellites broadcast radiofrequency carrier phase signals, they can potentially serve as promising candidates for augmenting GNSS PNT services. Due to their lower altitudes (300–2000 km), LEO satellites offer several advantages over their GNSS counterparts, which operate at altitudes exceeding 20,000 km. These advantages include stronger signal strength and more rapid geometric changes. For instance, the Iridium LEO constellation achieves a 25- to 30-dB improvement in signal-to-noise ratio compared to GNSS (Yang et al. 2024). Such LEO satellites can also pass overhead in just minutes, in contrast to the hours it takes for GNSS satellites (Ge et al. 2022; Shi et al. 2023). Studies on carrier phase tracking and positioning with these LEO constellations demonstrate that using a single LEO communication constellation—whether Iridium, Orbcomm,

✉ A. Khodabandeh
akhodabandeh@unimelb.edu.au

1 Department of Infrastructure Engineering, The University of Melbourne, Melbourne, Australia

2 School of Science, RMIT University, Melbourne, Australia

3 Department of Geoscience and Remote Sensing, Delft University of Technology, Delft, The Netherlands

Published online: 14 February 2025

OneWeb or Starlink—could achieve horizontal positioning accuracy of tens of meters for a single receiver (Orabi et al. 2021; Kozhaya et al. 2023). For the standalone Globalstar constellation, the results were less favorable, with Zhang et al. (2023) reporting horizontal accuracy of better than 300 m. With a combined LEO constellation, a horizontal accuracy of 5 m was obtained for a single receiver (Kozhaya et al. 2023).

In the aforementioned contributions, the achieved accuracy with multi-LEO constellations is only at the meter level, roughly hundreds of times less precise than what is expected by their carrier phase measurements. Next to inaccurate orbit products, this may be due to the treatment of LEO phase ambiguities as *real* values, discarding the important piece of information that such unknown ambiguities are constrained to be integer (Teunissen 1995). To fully leverage the ultra-precise phase measurements, one should therefore employ integer ambiguity resolution (IAR). While some studies have reported centimeter-level ambiguity-resolved positioning results using LEO simulation data (Li et al. 2019; Fang et al. 2024; Wang et al. 2024), these results are based on the assumption that LEO satellites broadcast both GPS-like phase and code signals employing the code division multiple access (CDMA) technique. However, as Table 1 indicates, most current LEO communication satellites transmit satellite-specific *frequency-varying* signals, which results in non-integer combinations of phase ambiguities when using the classical double-differencing technique (Khodabandeh and Teunissen 2023). By frequency-varying, here we mean that the frequencies are assumed to vary from transmitter to transmitter, while remaining unchanged over time. To address this, a new IAR theory for frequency-varying carrier phase measurements, like those of the GLONASS Frequency Division Multiple Access (FDMA) signals, was proposed by (Teunissen 2019). Numerical performance of the theory was studied in (Teunissen and Khodabandeh 2019; Hou et al. 2020; Brack et al. 2021; Zaminpardaz et al. 2021; Zhang et al. 2021). It is important to remark that there are also LEO satellites which transmit both code and phase measurements to support GNSS positioning, like the Luojia-1 scientific experimental satellite, the FutureNAV program from the European Space Agency (ESA), the PULSAR system from Xona Space Systems, and CENTISPACE™ system from Future Navigation (Wang et al. 2018b; Reid et al. 2022; Li et al. 2024; Xu et al. 2024). Here, we only consider communication LEO satellites with phase-only measurements.

In this contribution, we adopt the theory to investigate the performance of ambiguity-resolved positioning using LEO frequency-varying carrier phase measurements across various scenarios, such as varying cut-off elevations, numbers of satellites, and precision of carrier phase measurements. Although acquisition of carrier phase measurements from commercial LEO communication satellites is not a straightforward task, there exist contributions which have claimed the feasibility of obtaining such LEO-based measurements, see e.g., (Khalife and Kassas 2023) or (Kassas et al. 2024). It is important to note that acquiring such measurements requires a thorough understanding of their corresponding 'signal structure', without which the process would be quite challenging (Humphreys et al. 2023). Acknowledging the presence of this challenge, we *assume* LEO-based phase data acquisition is feasible in this paper. On the basis of such assumption, we therefore aim to conduct a *feasibility* study. To consider the realistic circumstance that most existing LEO communication satellites lack code measurements, a dual-epoch phase-only model is applied for baseline positioning (Teunissen 1997; Huisman et al. 2010; Wang et al. 2018a; Khodabandeh et al. 2021; Hou et al. 2022). This is achieved through a simulation platform we developed, which provides full control over the generation of parameters and measurements, followed by the estimation of the estimable parameters. A particular emphasis of this platform is its support for both standalone and combined LEO constellations, as well as the integration with real-world GNSS data. It is thereby shown that centimeter-level ambiguity-resolved positioning is possible under certain conditions, even with a satellite elevation cut-off angle of 50 degrees, making it suitable for GNSS-challenged environments like urban canyons.

The remainder of this contribution is organized as follows. Considering the *absence* of code data in LEO communication satellites, Sect. 2 highlights the crucial role of evaluating both satellite clock and orbital corrections in the linearization process of carrier phase observation equations. We state the necessary assumptions which must hold so as to make high-precision codeless positioning practical. While single-receiver high-precision positioning is challenged by inaccuracies in the LEO satellite orbit and clock products, it is shown that the relative distance between two receivers can help overcome this limitation. In Sect. 3, the dual-epoch phase-only model for relative short-baseline positioning is discussed and compared with the more commonly used GNSS single-epoch phase-and-code model. For the purpose of model comparison, some performance metrics, namely, the average positioning precision, average precision gain and the ambiguity dilution of precision (ADOP) (Teunissen 1997), are reviewed and provided with analytical expressions, illustrating the potential benefit of partial ambiguity-fixing in LEO-based phase-only positioning. Since every LEO constellation is shown to have its own distinct response to IAR, one may carry out a simulation study to assess the performance of the proposed phase-only model under several scenarios in which standalone and combined LEO constellations are assumed to transmit phase measurements at different precision levels. In Sect. 4, we therefore discuss the simulation platform developed for numerical analysis of LEO-based baseline positioning in detail. In Sect. 5, simu-

Table 1 Comparison of orbital parameters and signal structures for different communication LEO constellations used for Doppler positioning. Note that '*Starlink' in table only shows orbital parameters of Starlink first shell and '*Doppler frequencies' in table presents the tracking frequencies under real-world use in the literature as of the end of December 2023

	Iridium next	Orbcomm	Globalstar	OneWeb	*Starlink
Construction time	Iridium:1997-1998 NEXT:2017-2019	1997-1999	1998-1999	2019-2023	2019-ongoing
# of satellites	75	36	48	648	1440
# of orbital planes	6	6	8	12	72
# of satellites/planes	13	Plane A:8 Plane B:8 Plane C:8 Plane D:7 Plane F:2 Plane G:2	6	49	20
Inclination angle	86.4°	Plane A:45° Plane B:45° Plane C:45° Plane D:45° Plane F:70° Plane G:108°	52°	86.4°	53°
Altitude	∼ 780km	Plane A:∼815 km Plane B: ∼ 815km Plane C: ∼ 815km Plane D:∼815 km Plane F :∼740 km Plane G:785-875 km	∼1414 km	∼1200 km	∼550 km
Orbital period	∼100 min	∼100 min	∼114 min	∼109 min	∼96 min
Coverage	Global	Global	70° N − 70° S	Global	60° N − 60° S
Downlink signal spectrum	1626−1626.5 MHz (L-band)	137-138 MHz (VHF-band) 400.1 MHz (UHF-band)	2483.5-2500 MHz (S-band)	10.7−12.7 GHz (Ku-band)	10.7−12.7 GHz (Ku-band)
# of channels	5	12 on VHF-band 1 on UHF-band	13	8	8
*Doppler frequencies	1626.2708 MHz 1626.4375 MHz 1626.3958 MHz 1626.1458 MHz 1626.1042 MHz	137.2000 MHz 137.2250 MHz 137.2500 MHz 137.4400 MHz 137.4600 MHz 137.6625 MHz 137.6875 MHz 137.7125 MHz 137.7375 MHz 137.8000 MHz 137.2875 MHz 137.3125 MHz 400.1 MHz (UHF)	2484.39 MHz 2485.62 MHz 2486.85 MHz 2488.08 MHz 2489.31 MHz 2490.54 MHz 2491.77 MHz 2493.00 MHz 2494.23 MHz 2495.46 MHz 2496.69 MHz 2497.92 MHz 2499.15 MHz	10.825 GHz 11.075 GHz 11.325 GHz 11.575 GHz 11.825 GHz 12.075 GHz 12.325 GHz 12.575 GHz	10.825 GHz 11.075 GHz 11.325 GHz 11.575 GHz 11.825 GHz 12.075 GHz 12.325 GHz 12.575 GHz

lated LEO datasets under various conditions are analyzed to provide numerical insights into the partial-ambiguity-resolved positioning performance of LEO frequency-varying carrier phase signals. Next to the insights, we specifically explore the positioning capabilities of globally distributed short baselines using combined constellations including LEO and GNSS. A summary of the results and conclusions is given in Sect. 6.

2 Challenges of LEO phase-only positioning

In this section, we briefly review the important role played by the evaluation of both satellite clock and orbital corrections in the 'linearization' of carrier phase observation equations. Since these corrections have to be evaluated at the time that the phase signal is transmitted, one first requires to estimate *signal transmission time* for every receiver-satellite pair (Odijk 2017). Let t_r^s and τ_r^s denote the signal reception time and travel time corresponding to rover receiver r and satellite s, respectively. In the presence of GNSS pseudorange (code) data, standard single-point positioning can provide reception time estimate $\hat{t}_r^s$ and travel time estimate $\hat{\tau}_r^s$ with an accuracy level of several nanoseconds (de Jonge 1998, Chapter 2). As a result, the sought-for transmission time can be simply estimated as $\hat{t}_r^s - \hat{\tau}_r^s$. However, most existing LEO communication satellites do not provide code measurements. Here and in the following, we therefore assume that the rover receiver r does *not* have access to LEO code data. Instead, it relies on its carrier phase measurements as well as a nearby base receiver b which, in addition to LEO phase measurements, may have access to GNSS phase and code data. As will be shown in Sect. 3, the clock estimate of the rover is biased by the carrier phase ambiguities when using phase-only measurements. Under this condition, all the rover has at his disposal is to use the estimated reception time of the base receiver $\hat{t}_b^s$ and the travel time estimate $\hat{\tau}_r^s$ to approximate the transmission time $t_r^s - \tau_r^s$ as $\hat{t}_b^s - \hat{\tau}_r^s$. The implicit assumption for adopting such estimate is $t_r^s = t_b^s$. This assumption implies that the between-receiver single-differenced (SD) clock offset $dt_t = t_r^s - t_b^s$ should be *discarded* when the signals at both receivers are deemed to be received *simultaneously*, at least during the linearization stage. We investigate, under what conditions, this assumption is plausible for short-baseline ambiguity-resolved positioning.

Let the m-vector ϕ_t contain between-receiver SD carrier phase measurements that are collected by a pair of receivers tracking simultaneously m satellites at epoch t. Assuming that the distance between the two receivers is sufficiently short to neglect the SD atmospheric delays, the corresponding system of *linearized* observation equations reads (Odijk 2017)

$$\mathsf{E}(\phi_t) - \bar{\phi}_t(x_r^\circ, t_b, t_r, \tau_b, \tau_r) = \bar{G}_t\, \Delta x + e\, dt_t + \Lambda\, a \tag{1}$$

with the expectation operator $\mathsf{E}(\cdot)$, and the subscripts b and r denoting the base and rover receiver indexes, respectively. The dependency of the 'computed' measurement vector $\bar{\phi}_t = [\bar{\phi}_t^s]\,(s = 1, \ldots, m)$ on the *approximate* rover position vector x_r°, signal reception time vectors $t_b = [t_b^s]$ and $t_r = [t_r^s]$, and the signal travel time vectors $\tau_b = [\tau_b^s]$ and $\tau_r = [\tau_r^s]$ is characterized by

$$\begin{aligned}\bar{\phi}_t^s = {} & dt^s(t_r^s - \tau_r^s) - dt^s(t_b^s - \tau_b^s) \\ & + ||x_r^\circ - x^s(t_r^s - \tau_r^s)|| - ||x_b - x^s(t_b^s - \tau_b^s)||\end{aligned} \tag{2}$$

in which the base position vector is assumed to be known and given by x_b. The notation $[\bullet]$ indicates a vector (or matrix) containing scalar (or vector) $\bullet$. Likewise, the satellite position vectors (after Earth rotation corrections) are given by x^s $(s = 1, \ldots, m)$. The satellite clock offset is denoted by dt^s. The $m \times 3$ matrix $\bar{G}_t = [\,\bar{g}_t^s\,]$ contains satellite-to-rover line-of-sight (LOS) direction vectors

$$\bar{g}_t^s = \left(x_r^\circ - x^s(t_r^s - \tau_r^s)\right) / ||x_r^\circ - x^s(t_r^s - \tau_r^s)||, \tag{3}$$

linking the unknown rover position increment vector $\Delta x = x_r - x_r^\circ$ to the measurements. The unknown SD receiver clock offset is given by dt_t, with e being the m-vector of ones. The $m \times m$ diagonal matrix $\Lambda = \mathrm{diag}(\lambda_1, \ldots, \lambda_m)$ contains the satellite-specific wavelength λ_s, serving as the design matrix of the SD ambiguity vector a. The SD receiver phase bias is lumped with the real-valued ambiguity vector a. Note that both the ambiguity vector a and the increment vector Δx do not have the epoch index t as their subscript because they are assumed to be constant over time. Apart from a that is expressed in cycles, all the other quantities in (1) are expressed in units of length.

The system of equations (1) shows that the estimation of the unknown parameter vectors Δx_r, dt_t, and a is driven by the computed measurement vector $\bar{\phi}_t$. Evaluation of $\bar{\phi}_t$, on the other hand, relies on the signal reception time vectors t_r and t_b, and the travel time vectors τ_r and τ_b, which are *unknown* in principle. In practice, one therefore has to use their estimates, say $\hat{t}_r$, $\hat{t}_b$, $\hat{\tau}_r$ and $\hat{\tau}_b$, to evaluate $\bar{\phi}_t$. By doing so, the observation equations (1) are replaced by

$$\mathsf{E}(\Delta\phi_t) = G_t\, \Delta x + e\, dt_t + \Lambda\, a + \varepsilon_t \tag{4}$$

with $\Delta\phi_t = \phi_t - \bar{\phi}_t(x_r^\circ, \hat{t}_b, \hat{t}_r, \hat{\tau}_b, \hat{\tau}_r)$, and the bias vector $\varepsilon_t = \bar{\phi}_t(x_r^\circ, t_b, t_r, \tau_b, \tau_r) - \bar{\phi}_t(x_r^\circ, \hat{t}_b, \hat{t}_r, \hat{\tau}_b, \hat{\tau}_r)$. Note, in (4), that matrix $\bar{G}_t$ is approximated by the $m \times 3$ matrix $G_t = [\,g_t^s\,]$ containing the LOS direction vectors (compare with 3)

$$g_t^s = \left(x_r^\circ - x^s(\hat{t}_r^s - \hat{\tau}_r^s)\right) / ||x_r^\circ - x^s(\hat{t}_r^s - \hat{\tau}_r^s)||, \tag{5}$$

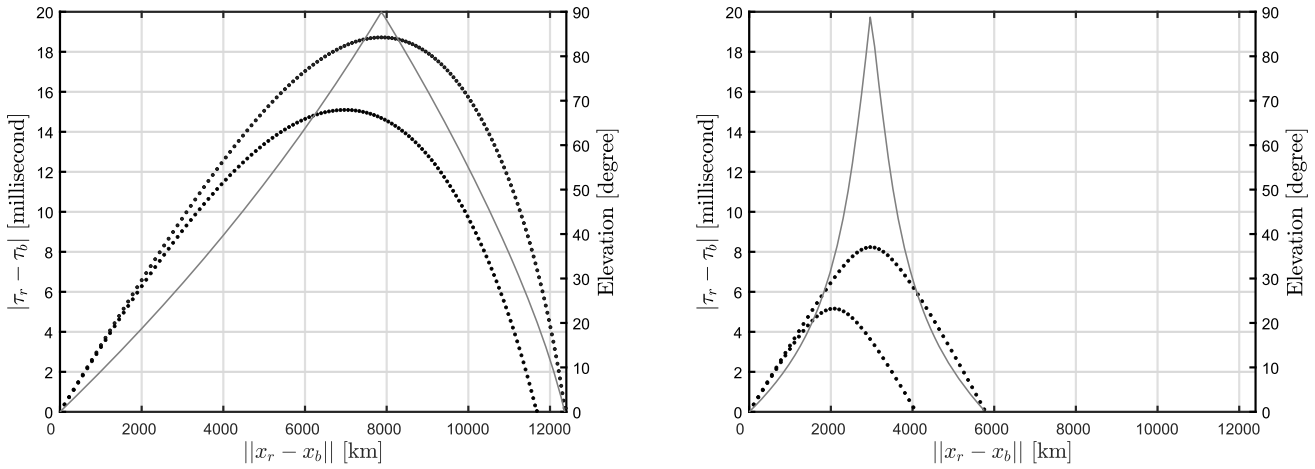

Fig. 1 Maximum values of the signal travel time difference $|\tau_r^s - \tau_b^s|$ [millisecond] as a function of the baseline length $||x_r - x_b||$ [km] that is experienced by the rover and base receivers tracking GPS satellite PRN 1 (left) and Iridium satellite I103 (right). The cut-off elevation is to zero (upper dotted curves) and 10 degrees (lower dotted curves). The base receiver is observing the satellite at an elevation equal to the cut-off, while the rover receiver is observing it at an elevation depicted by the gray lines

The presence of the bias vector ε_t would challenge the applicability of (4) for positioning, particularly when the magnitude of ε_t is deemed to be significantly larger than the millimeter-level noise of the carrier phase measurements ϕ_t. In the following, we therefore discuss the contributing factors in ε_t and make necessary assumptions about these terms so as to be able to neglect the presence of ε_t in (4). Each of the entries of the bias vector $\varepsilon_t = [\varepsilon_t^s]$ can be shown to be, up to the first-order term, decomposed into three parts (Appendix A)

$$\varepsilon_t^s = \mathrm{I} + \mathrm{II} + \mathrm{III} \tag{6}$$

The first part I concerns the satellite clock stability and reads

$$\mathrm{I} = [dt^s(t_r^s - \tau_r^s) - dt^s(t_b^s - \tau_b^s)] - [dt^s(\hat{t}_r^s - \hat{\tau}_r^s) - dt^s(\hat{t}_b^s - \hat{\tau}_b^s)] \tag{7}$$

While both the base and rover receivers aim to *simultaneously* track the satellites, their clocks can be unsynchronized, meaning that the difference between their signal reception times is given by the *nonzero* SD receiver clock offset, that is, $dt_t = t_r^s - t_b^s$ $(s = 1, \ldots, m)$. Let us set the estimates as $\hat{t}_r^s = \hat{t}_b^s$ and $\hat{\tau}_r^s = \hat{\tau}_b^s$. This is realized if the SD receiver clock estimate, say $d\hat{t}_t = \hat{t}_r^s - \hat{t}_b^s$, is taken to be zero. If we also assume that the signal travel times, experienced by the base and rover receivers, are almost identical $(\tau_r^s \approx \tau_b^s)$, (7) simplifies to $\mathrm{I} = dt^s(t_b^s - \tau_b^s + dt_t) - dt^s(t_b^s - \tau_b^s)$. Although Frequency Electronics, Inc. (FEI) have published that the stability of its Master Oscillator Timing/Frequency Generation unit, which is provided to the Iridium NEXT satellites, is roughly 10^{-10} sec/sec over short time intervals, e.g. 0.001 s (Bloch et al. 2012), the stability of most commercial LEO communication satellites' clocks and their synchronicity are unknown (Kassas et al. 2021). Khairallah and Kassas (2022) suggested that the Orbcomm clocks have comparable stability to a typical temperature compensated crystal oscillator (TCXO), which can reach a short-term stability of 10^{-12} sec/sec (Teunissen and Montenbruck 2017). The Starlink satellites were assumed to be equipped with chip-scale atomic clocks (CSACs) (Saroufim et al. 2023; Hayek et al. 2023; Khalife and Kassas 2023), with short-term stability ranging from 10^{-13} sec/sec to 10^{-12} sec/sec (Rybak et al. 2021).

The clock of most GNSS receivers and high-end software-defined radios can ensure such bounded offsets. However, the assumption of having identical signal travel times is only plausible when the distance between the rover and base receivers (baseline length) is not too large. Figure 1 shows the maximum difference $|\tau_r^s - \tau_b^s|$ as a function of the baseline length $||x_r - x_b||$ for a GNSS-case (left) and a LEO-case (right). As shown, the magnitude $|\tau_r^s - \tau_b^s|$ is less than 4 milliseconds for baselines less than 1000 km. For much shorter baselines, e.g. less than 10 km, this difference becomes less than several tens of microseconds. Therefore, the conclusion reads that the clock bias term I can be neglected for not-too-large baselines even when one has *no* access to a data-driven estimate of the SD clock offset dt_t, i.e., $d\hat{t}_t = 0$.

The second and third parts II and III in (6) concern the time change in the satellite orbits. Let us first consider Part II. It reads

$$\mathrm{II} = \left(\frac{v_r^s - v_b^s}{c}\right)([\hat{t}_b^s - t_b^s] - [\hat{\tau}_b^s - \tau_b^s]) \tag{8}$$

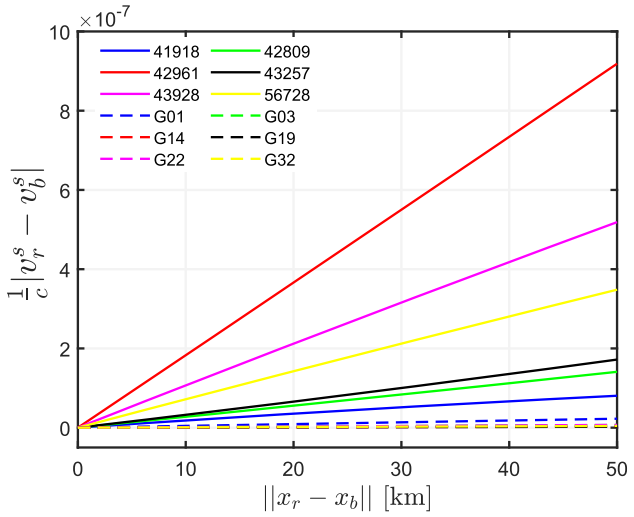

Fig. 2 Examples of the absolute values of $(v_r^s - v_b^s)/c$ as a function of the baseline length $||x_r - x_b||$ [km] for Iridium satellites (solid lines), and for GPS satellites (dashed lines). The legend displays the NORAD numbers of the Iridium satellites and the PRNs of the GPS satellites

with c being the speed of light, where v_r^s and v_b^s denote the satellite LOS velocities with respect to the rover and base receivers, respectively. Accordingly, the shorter the baseline length, the more similar the satellite-to-receiver LOS directions of the rover and base receivers, thereby the smaller (in magnitude) the velocity difference $v_r^s - v_b^s$ becomes. The impact of the difference $v_r^s - v_b^s$ in Ⅱ can be further attenuated if the estimation errors $\hat{t}_b^s - t_b^s$ and $\hat{\tau}_b^s - \tau_b^s$ are small. As stated earlier, if the role of the base receiver is taken by a CORS station with access to GNSS code (pseudorange) measurements, single-point positioning of the base receiver leads to the clock offset estimate $\hat{t}_b^s$ and travel time estimate $\hat{\tau}_b^s$ with an accuracy of several nanoseconds. Under such assumption, Part Ⅱ is roughly equal to $(v_r^s - v_b^s)/c$ times several decimeters. Figure 2 shows absolute values of $(v_r^s - v_b^s)/c$, corresponding to GPS and Iridium satellites, as a function of the baseline length $||x_r - x_b||$. Due to the low altitude of Iridium LEO satellites (Table 1), their corresponding values are almost one order of magnitude larger than their GPS counterparts. For baselines less than 10 km, the absolute value $|v_r^s - v_b^s|/c$ is less than 2×10^{-7}, making Ⅱ less than 0.002 mm. Considering the mm-level precision of carrier phase data, this bias term can also be neglected.

So far, under the assumption of having sufficiently short baselines with stable satellite clocks, it is shown that the first two parts I and Ⅱ in (6) can be neglected. What left to consider is the last part, i.e.,

$$\text{Ⅲ} = \frac{v_r^s}{c}\left([\tau_r^s - \hat{\tau}_r^s] - [\tau_b^s - \hat{\tau}_b^s] + [d\hat{t}_t - dt_t]\right) \tag{9}$$

As the rover is assumed to have no access to code data, the estimate of the clock offset dt_t may be taken as zero, i.e.,

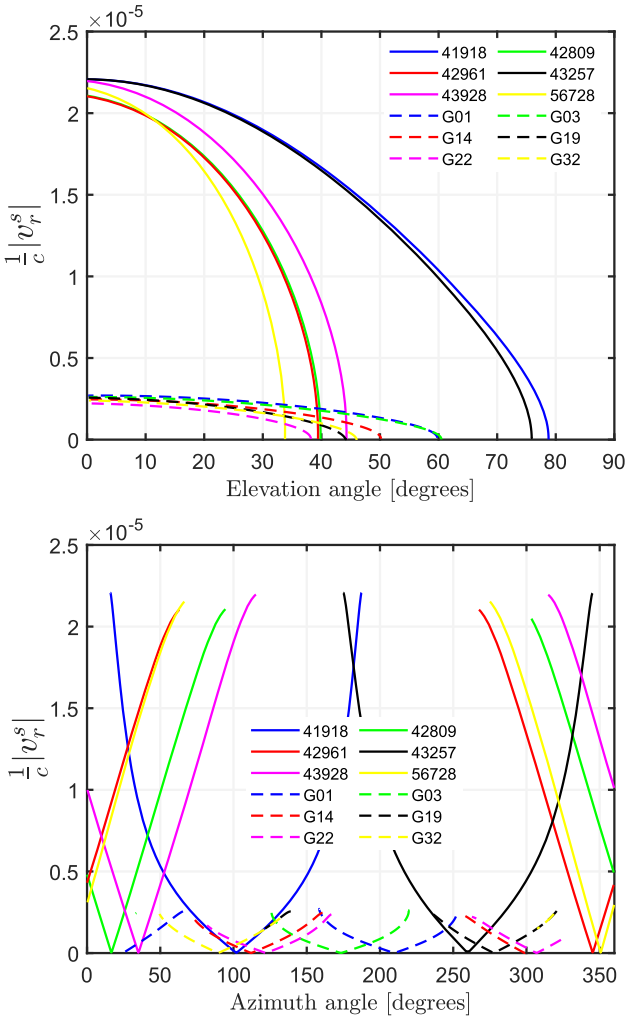

Fig. 3 Examples of the absolute values of v_r/c as a function of satellite elevation (top) and azimuth (bottom), observing Iridium satellites (solid lines) and GPS satellites (dashed lines), respectively. The legend displays the NORAD numbers for Iridium satellites and the PRNs for GPS satellites

$d\hat{t}_t = 0$. This, together with discarding the nanosecond-level estimation error $[\tau_b^s - \hat{\tau}_b^s]$, simplifies the last part as Ⅲ $= (v_r^s/c)(\tau_r^s - \hat{\tau}_r^s - dt_t)$. In contrast to the two previous bias parts I and Ⅱ for which the baseline length is leveraged, the bias term $(v_r/c)dt_t$ cannot be mitigated by choosing short baselines. As will be shown in Sect. 3, our phase-only model can deliver a meter-level ambiguity-float estimate for the rover position x_r°. This leads to signal travel estimates $\hat{\tau}_r^s$ $(s = 1, \ldots, m)$ with an accuracy of several nanoseconds (cf. Figure 1). Neglecting the estimation error $[\tau_r^s - \hat{\tau}_r^s]$, the term Ⅲ is therefore mainly driven by the SD receiver clock offset dt_t and the satellite LOS velocity vector $v_r = [v_r^s]$. Figure 3 shows absolute values of v_r^s/c as a function of both satellite elevation (top) and azimuth (bottom) angles for GPS and Iridium satellites. For the GPS-case, $|v_r^s|/c$ does not exceed 2.2×10^{-6}. For the Iridium-case however, this upper-bound

gets 10 times larger, i.e., 2.2×10^{-5}. Therefore, if the absolute value of the SD clock offset dt_t does not exceed 1 microsecond, the bias term $|(v_r^s/c)dt_t|$ would then be bounded by 7 mm. This bias clearly cannot be neglected. In the following, we therefore assume that the SD clock offset is less than 0.1 microseconds so as to neglect the presence of the bias vector ε_t in (4).

We conclude this section by making a remark about satellite orbital biases. By considering sufficiently short baselines and having receivers equipped with high-grade clocks, the bias vector ε_t was shown to be discarded. This, however, relies on a crucial assumption of having precise satellite orbit products x^s $(s = 1, \ldots, m)$. As shown in Appendix B, the presence of five-meter bias vectors in GPS satellite orbits leads to between-receiver SD range biases smaller than 0.8 mm for baselines shorter than 5 km. However, the presence of such biases in Iridium and OneWeb LEO satellite orbits can lead to SD range biases as large as 12 mm whose effect on the rover positioning solution is less than 6 mm (cf. Figure 16 in Appendix B). This shows the prominent role of orbit products in LEO-based positioning (Allahvirdi-Zadeh et al. 2022). In the following, we assume that the LEO satellite orbit products are precise enough so as to neglect the impact of such orbital biases.

3 Phase-only and phase-and-code models compared

Given the approximation $\varepsilon_t \approx 0$, the system of phase observation equations (4) is revised as

$$\mathsf{E}(\Delta\phi_t) = G_t\,\Delta x + e\,dt_t + \Lambda\,a \tag{10}$$

As the number of SD ambiguities a is as many as the number of the measurements, the measurement vector $\Delta\phi_t$ is fully reserved for a, meaning that none of the parameter vectors Δx, dt_t and a can be unbiasedly determined via (10). One would therefore need to augment the underdetermined system (10) by additional observation equations. In the context of GNSS positioning, such equations are made available by the presence of GNSS code data. In the case of LEO communication satellites however, code data may be absent, urging one to use phase data of further epochs. For the sake of comparison, we first present a more commonly used GNSS model, i.e., the single-epoch phase-and-code model, see e.g. (Odolinski et al. 2015) or (Zaminpardaz et al. 2021). This will then be followed by a lesser-known model, i.e., the dual-epoch phase-only model (Teunissen 1997; Khodabandeh et al. 2021) which can potentially be employed for LEO frequency-varying carrier phase signals.

3.1 Single-epoch phase-and-code model

Let the m-vector p_t be the code counterpart of the SD phase measurement vector ϕ_t. As with $\Delta\phi_t$, one can form the observed-minus-computed vector $\Delta p_t = p_t - \bar{\phi}_t(x_r^\circ, \hat{t}_b, \hat{t}_r, \hat{\tau}_b, \hat{\tau}_r)$. The corresponding observation equations can be augmented with (10) as follows

$$\mathsf{E}\left(\begin{bmatrix}\Delta\phi_t\\ \Delta p_t\end{bmatrix}\right) = \begin{bmatrix}G_t\\ G_t\end{bmatrix}\Delta x + \begin{bmatrix}e\\ e\end{bmatrix}\overbrace{(dt_t + d)}^{d\tilde{t}_t} + \begin{bmatrix}\Lambda\\ 0\end{bmatrix}\underbrace{(a - \Lambda^{-1}e\,d)}_{\tilde{a}} \tag{11}$$

with d being the SD receiver code bias and the joint variance matrix

$$\mathsf{D}\left(\begin{bmatrix}\Delta\phi_t\\ \Delta p_t\end{bmatrix}\right) = \begin{bmatrix}Q_{\phi_t\phi_t} & 0\\ 0 & Q_{p_tp_t}\end{bmatrix} \tag{12}$$

The $m \times m$ variance matrices $Q_{\phi_t\phi_t}$ and $Q_{p_tp_t}$ are specified as

$$\begin{cases} Q_{\phi_t\phi_t} = 2\,\sigma_\phi^2\,\Lambda\,W_t^{-1}\Lambda \\ Q_{p_tp_t} = 2\,\sigma_p^2\,W_t^{-1} \end{cases} \tag{13}$$

The SD code bias d cannot be estimated by the model (11). Instead, it is absorbed by both the estimable receiver clock $d\tilde{t}_t = dt_t + d$ and estimable ambiguity vector $\tilde{a} = a - \Lambda^{-1}e\,d$. The zenith-referenced standard deviation of the undifferenced (UD) phase data, expressed in *cycles*, is denoted by σ_ϕ. Its code counterpart, expressed in units of length, is given by the scalar σ_p. Since the phase signals are frequency-varying, every satellite s may send phase measurement ϕ_t^s with a precision that is inversely proportional to the underlying wavelength λ_s, that is $\sigma_{\phi^s} = \sigma_\phi\lambda_s$. The square value of the wavelength λ_s in the phase variance $\sigma_{\phi^s}^2 = \sigma_\phi^2\lambda_s^2$ explains why the wavelength matrix Λ appears twice in $Q_{\phi_t\phi_t}$. Furthermore, both the phase and code data generally become less precise the smaller the satellite elevation becomes. Therefore, the $m \times m$ diagonal weight matrix W_t models the elevation-dependency of the data. Also note that the presence of the number 2 in (13) indicates that the variance of the SD measurements is twice that of their UD counterparts, assuming that the measurements of the rover and base receivers are uncorrelated.

The phase-and-code model (11) is solvable and delivers unbiased solutions for the parameter vectors Δx, $d\tilde{t}_t$ and $\tilde{a}$, if the $m \times 4$ matrix $[G_t, e]$ is of full-column rank (Teunissen 1997). The necessary condition is to track at least 4 satellites $(m \geq 4)$.

3.2 Dual-epoch phase-only model

In the absence of the code data p_t, one can augment the phase data ϕ_t by its counterpart collected at the next epoch $t+1$, taking advantage of the fact the ambiguities a remain time-constant if no phase cycle-slip occurs. Accordingly, the dual-epoch phase-only model is given by

$$\mathsf{E}\left(\begin{bmatrix}\Delta\phi_t\\ \Delta\phi_{t+1}\end{bmatrix}\right) = \begin{bmatrix}G_t\\ G_{t+1}\end{bmatrix}\Delta x + \begin{bmatrix}0\\ e\end{bmatrix}\overbrace{(dt_{t+1}-dt_t)}^{d\tilde{t}_{t+1}} + \begin{bmatrix}\Lambda\\ \Lambda\end{bmatrix}\underbrace{(a+\Lambda^{-1}e\,dt_t)}_{\tilde{a}} \tag{14}$$

with the joint variance matrix

$$\mathsf{D}\left(\begin{bmatrix}\Delta\phi_t\\ \Delta\phi_{t+1}\end{bmatrix}\right) = \begin{bmatrix}Q_{\phi_t\phi_t} & 0\\ 0 & Q_{\phi_{t+1}\phi_{t+1}}\end{bmatrix} \tag{15}$$

Compare (14) with (11). The role of the code measurement vector Δp_t is taken by $\Delta\phi_{t+1}$. Importantly, the phase-only model (14) fails to estimate the SD receiver clock offset dt_t. Instead, the between-epoch difference $d\tilde{t}_{t+1} = dt_{t+1} - dt_t$ can be estimated. This is because the clock offset dt_t is absorbed by the phase ambiguity vector a to form the estimable SD ambiguities $\tilde{a} = a + \Lambda^{-1}e\,dt_t$. With the phase-only model (14), the epoch-average of the phase data $\Delta\phi_t$ and $\Delta\phi_{t+1}$ is reserved for the estimable ambiguities $\tilde{a}$. Therefore, it is the between-epoch difference $\Delta\phi_{t+1} - \Delta\phi_t$ which determines the ambiguity-float solutions for Δx and $d\tilde{t}_{t+1}$. As a result, the model becomes solvable if the $m \times 4$ matrix $[G_{t+1} - G_t, e]$ is of full-column rank (Teunissen 1997). The necessary condition is to track at least 4 satellites ($m \geq 4$), while experiencing time changes in the receiver-to-satellite LOS directions, i.e., $G_{t+1} - G_t \neq 0$.

3.3 Integer-estimable combinations of the ambiguities

Given the phase-and-code model (11) or the phase-only model (14), one can employ the minimum-variance least-squares estimation to obtain the so-called *float* estimators of the estimable ambiguity vector $\tilde{a} \in \mathbb{R}^m$ and the rover position vector $x \in \mathbb{R}^3$. Let such float estimators and their joint variance matrix be denoted by

$$\begin{bmatrix}\hat{a}\\ \hat{x}\end{bmatrix}, \begin{bmatrix}Q_{\hat{a}\hat{a}} & Q_{\hat{a}\hat{x}}\\ Q_{\hat{x}\hat{a}} & Q_{\hat{x}\hat{x}}\end{bmatrix} \tag{16}$$

The word 'float' is used to emphasize that the above solutions do *not* benefit from the extra information that combinations of the estimable ambiguity vector $\tilde{a}$ are *integer-valued*. In both the models (11) and (14), the estimable ambiguity vector $\tilde{a}$ takes the form of $\tilde{a} = a + \Lambda^{-1}e\,b$, where the role of the non-integer bias $b \in \mathbb{R}$ is taken by the SD phase/code biases and/or by the SD receiver clock offsets. The task is to identify the combinations $z = F^T\tilde{a}$ in which the full-rank integer matrix $F \in \mathbb{Z}^{m\times(m-1)}$ should nullify the non-integer term $\Lambda^{-1}e\,b$, that is, $F^T\Lambda^{-1}e = 0$. To identify such combinations, let us first work out the $m \times m$ diagonal wavelength matrix Λ. As the last rows of Table 1 indicate, the signal frequencies of each LEO constellation are *integer* multiples of a base frequency. For instance, in the case of Iridium, satellite frequencies $f_s = c/\lambda_s$ ($s = 1, \ldots, m$) are related to their base frequency f_0 as

$$\begin{aligned}&f_s = r_s\,f_0, \quad (f_0 = 100\text{ Hz}) \text{ with}\\ &r_s \in \{16261042, 16261458, 16262708, 16263958, 16264375\}\end{aligned} \tag{17}$$

Defining the base wavelength $\lambda_0 = c/f_0$, the wavelength matrix can be expressed as $\Lambda = \lambda_0 R^{-1}$, where the diagonal matrix $R = \text{diag}(r_1, \ldots, r_m)$ contains the integer ratios r_s. Substitution into $\tilde{a} = a + \Lambda^{-1}e\,b$ gives

$$\tilde{a} = a + Re\,\frac{b}{\lambda_0} \tag{18}$$

The integer matrix F should then satisfy the two conditions of *integer-estimability* (Teunissen 2019), that is, it should 1) satisfy $F^T Re = 0$, and 2) be equal to rows of an $m \times m$ admissible ambiguity transformation. The first condition is to ensure that the function $z = F^T\tilde{a}$ does not contain the non-integer bias b, while the second condition is to ensure that the integerness of z aligns with the integer values of the original ambiguities a that the function is applied to. Such matrix can be obtained by an application of the integer-sweeping algorithm (Teunissen and Khodabandeh 2022, pp. 5). In doing so, we assume that the greatest common divisor (GCD) of the ratios r_s is one, as with the GCD of the ratios r_s in (17). For the cases where the GCD is larger than one, the ratios can be down-scaled by being divided by their GCD. As an example, consider the ratios in (17). Given the input vector $Re = [r_1, r_2, r_3, r_4, r_5]^T$ ($m = 5$), the algorithm returns the following output matrix

$$F^T = \begin{bmatrix}39063, & -39053, & -9, & 0, & 0\\ -625, & 833, & -208, & 0, & 0\\ 0, & 1, & -2, & 1, & 0\\ 1, & -4, & 5, & 0, & -2\end{bmatrix} \tag{19}$$

It can be verified that $F^T Re = 0$, and that the matrix F is part of the admissible ambiguity transformation $[F, h]$, with $h = [1,\ 0,\ -2,\ 0,\ 1]^T$. Using matrix F, integer ambiguity resolution (IAR) methods like LAMBDA (Teunissen 1995)

can be employed to take the real-valued float ambiguity solution $\hat{z} = F^T\hat{a}$ and its variance matrix $Q_{\hat{z}\hat{z}} = F^T Q_{\hat{a}\hat{a}} F$ as input, returning the integer-valued *fixed* ambiguity solution $\check{z} \in \mathbb{Z}^{(m-1)}$ as output. If the probability that the float ambiguities are mapped to their correct integers is close to one, the fixed estimator of the rover position vector $x \in \mathbb{R}^3$ and its variance matrix can be evaluated as (ibid)

$$\begin{aligned} \check{x} &= \hat{x} - Q_{\hat{x}\hat{a}} F (F^T Q_{\hat{a}\hat{a}} F)^{-1} (\hat{z} - \check{z}) \\ Q_{\check{x}\check{x}} &= Q_{\hat{x}\hat{x}} - Q_{\hat{x}\hat{a}} F (F^T Q_{\hat{a}\hat{a}} F)^{-1} F^T Q_{\hat{a}\hat{x}} \end{aligned} \tag{20}$$

3.4 Performance metrics

The second equation in (20) indicates that the precision of the position solution can be improved by accounting for the integer constraint $z \in \mathbb{Z}^{(m-1)}$. This is the case if the covariance matrix between the float position solution $\hat{x}$ and the float ambiguity solution $\hat{z}$, i.e., $Q_{\hat{x}\hat{z}} = Q_{\hat{x}\hat{a}} F$, contains nonzero entries. In the extreme case $Q_{\hat{x}\hat{z}} = 0$, i.e., when $\hat{x}$ and $\hat{z}$ are uncorrelated, no precision improvement is experienced by IAR. As far as the precision of the position solution is concerned, one therefore needs to address the following three questions

1. Given the precision of the float position solution, is IAR required?
2. How much does IAR improve the precision of the position solution?
3. Given the underlying model, is IAR feasible?

The answer to the first question lies in the variance matrix $Q_{\hat{x}\hat{x}}$, while the second question can be addressed by comparing $Q_{\check{x}\check{x}}$ relative to $Q_{\hat{x}\hat{x}}$. The third (last) question should be addressed using the ambiguity variance $Q_{\hat{a}\hat{a}}$. We first take a measure for addressing the first question. Recall that the variance of a linear function of the float position solution $\hat{x}$, say $f^T\hat{x}$ ($f \in \mathbb{R}^3$), is given by the scalar $f^T Q_{\hat{x}\hat{x}} f$. When $||f|| = 1$, the smallest and largest values that the variance $f^T Q_{\hat{x}\hat{x}} f$ can take are the minimum and maximum eigenvalues of $Q_{\hat{x}\hat{x}}$, respectively (Teunissen 1997). As such, the geometric average of the eigenvalues of $Q_{\hat{x}\hat{x}}$, i.e., the cube root of its determinant, represents the average variance of $\hat{x}$. By taking the square root of the average variance, we thus arrive at

$$\text{1. Average precision of } \hat{x}: \ \bar{\sigma}_{\hat{x}} = \sqrt{|Q_{\hat{x}\hat{x}}|}^{\frac{1}{3}} \tag{21}$$

The average precision $\bar{\sigma}_{\hat{x}}$ is in units of length. Depending on the positioning application and the magnitude of $\bar{\sigma}_{\hat{x}}$ (e.g. cm-level to meter-level), one can decide if IAR is required or not.

A measure for addressing the second question can be given by the concept of *precision gain* (Teunissen 1997). The precision gain by IAR for the function $f^T x$ is given by the variance ratio $f^T Q_{\hat{x}\hat{x}} f / f^T Q_{\check{x}\check{x}} f$. This variance ratio is bounded from below by one. As with the average variance, its smallest and largest values are equal to the minimum and maximum eigenvalues of $Q_{\hat{x}\hat{x}} Q_{\check{x}\check{x}}^{-1}$. Likewise, the cube root of the determinant ratio $|Q_{\hat{x}\hat{x}}|/|Q_{\check{x}\check{x}}|$ represents the average variance ratio. By taking the square root of the average variance ratio, we arrive at

$$\text{2. Average precision gain of } \hat{x}: \ \mathcal{G}_{\hat{x}} = \frac{\bar{\sigma}_{\hat{x}}}{\bar{\sigma}_{\check{x}}} \tag{22}$$

The average precision gain $\mathcal{G}_{\hat{x}}$ tells us how many times the average precision of the fixed position solution $\check{x}$ is smaller than that of its float counterpart $\hat{x}$. When $\mathcal{G}_{\hat{x}}$ is close to one, it implies that no considerable precision improvement is realized by IAR. On the other hand, large values of $\mathcal{G}_{\hat{x}}$ indicates considerable precision improvement.

The last question concerns whether or not the integer mapping $\hat{z} \mapsto \check{z}$ is successful in the sense of having the fixed solution $\check{z}$ equal to the true integer vector $z = F^T\tilde{a}$. Whether or not IAR is deemed successful is determined by the probability of correct integer estimation, the so-called ambiguity success-rate (Teunissen 1999). As an indication of the ambiguity success-rate, we use the ambiguity dilution of precision (ADOP). Like (21), the ADOP is defined as the average precision of the float ambiguities $\hat{z} \in \mathbb{R}^{(m-1)}$, that is (Teunissen 1997)

$$\text{3. ADOP}: \ \bar{\sigma}_{\hat{z}} = \sqrt{|Q_{\hat{z}\hat{z}}|}^{\frac{1}{(m-1)}} \tag{23}$$

The ADOP $\bar{\sigma}_{\hat{z}}$ is in cycles. From the ADOP, one can infer an upper bound for the bootstrapped ambiguity success-rate. The smaller the ADOP, the higher the upper bound of the success rate becomes. For ADOP smaller than 0.14 cycles, the stated upper bound is always higher than 99% (Odijk and Teunissen 2008). The following lemma presents expressions for the three performance metrics (21), (22), and (23) of the phase-and-code (PC) model.

Lemma 1 (Performance of the PC model) *With respect to the PC model (11), the average precision $\bar{\sigma}_{\hat{x}}$, precision gain $\mathcal{G}_{\hat{x}}$, and the ADOP $\bar{\sigma}_{\hat{z}}$ can be expressed as*

$$\begin{aligned} \bar{\sigma}_{\hat{x}} &= \frac{\sqrt{2}\,\sigma_p}{\sqrt{m}\,\sigma_G}, \quad \sigma_G^2 = \tfrac{1}{m}|G_t^T W_t P G_t|^{\frac{1}{3}} \\ \mathcal{G}_{\hat{x}} &\approx \iota \frac{\sigma_p}{\lambda\,\sigma_\phi} \\ \bar{\sigma}_{\hat{z}} &= \sqrt{2}\,\sigma_\phi\, \sqrt{m}^{\,\frac{1}{m-1}}\, \mathcal{G}_{\hat{x}}^{\frac{3}{m-1}}\, r^{\frac{1}{m-1}} \end{aligned} \tag{24}$$

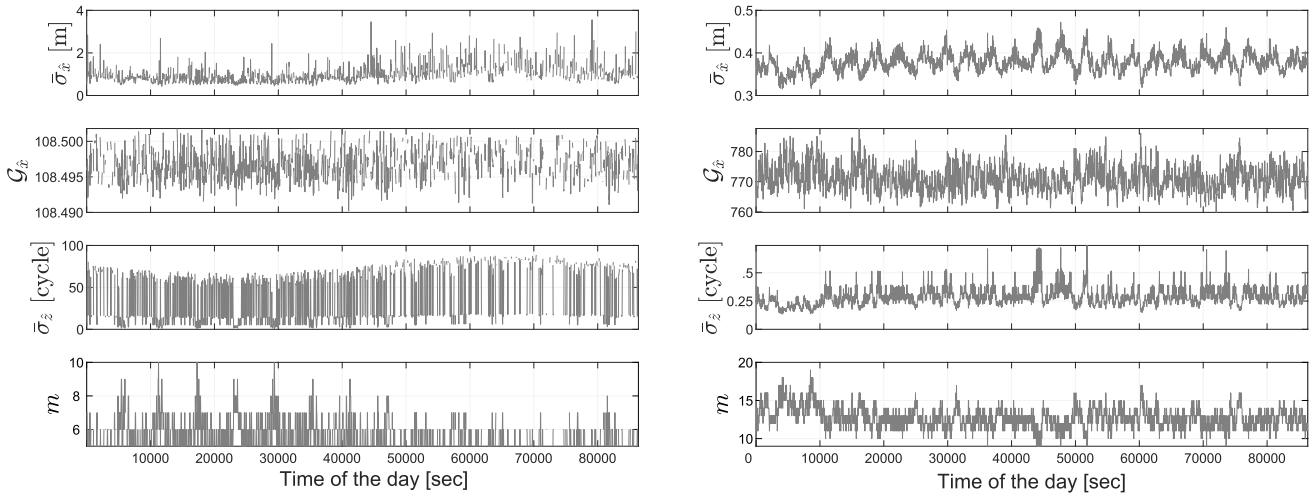

Fig. 4 Performance metrics of the PC model for the Iridium (left) and OneWeb (right) satellites: examples of the average precision $\bar{\sigma}_{\hat{x}}$ (1st row), precision gain $\mathcal{G}_{\hat{x}}$ (2nd row), and the ADOP $\bar{\sigma}_{\hat{z}}$ (3rd row), together with the number of tracked satellites m (4th row) over one day (19th of December, 2023). The location of the 5-km baseline is in CANADA (left: station ALRT) and China (right: station BJNM). The zenith-reference code and phase standard deviations are set to $\sigma_p = 0.2$ [m] and $\sigma_\phi = 0.01$ [cycle], respectively

where

$$\iota = \left(\frac{\sqrt{|G_t^T \bar{W}_t \bar{P} G_t|}}{\sqrt{|G_t^T W_t P G_t|}} \right)^{\frac{1}{3}} \tag{25}$$

with $\bar{W}_t = (1/r^2) R W_t R$, $\lambda = \lambda_0 / r$, *and* $r = (\prod_{s=1}^{m} r_s)^{\frac{1}{m}}$. *The scalar* $\bar{m}$ *reads* $\bar{m} = \text{trace}(\bar{W}_t)/|W_t|$. *The two projectors* P *and* $\bar{P}$ *are given by* $P = I_m - (1/e^T W_t e) e e^T W_t$ *and* $\bar{P} = I_m - (1/e^T \bar{W}_t e) e e^T \bar{W}_t$.

Proof The proof, together with the exact expression of $\mathcal{G}_{\hat{x}}$, is given in Appendix A. □

The first expression of (24) shows that the average precision of the float position solution $\hat{x}$ is driven by the standard deviation of the SD code data Δp_t, i.e., by $\sqrt{2}\,\sigma_p$, for the PC model. The role of the phase data $\Delta\phi_t$ is absent because they are all reserved to determine the estimable ambiguities $\tilde{a}$ in (11). The more precise the code data, the smaller the variance σ_p^2, thus the smaller the average precision $\bar{\sigma}_{\hat{x}}$ becomes. The first expression also shows the important role played by the *dispersion* of the receiver-to-satellite LOS directions in G_t with respect to their average, i.e., the scalar σ_G. To see this, consider the functionality of the projector P. By pre-multiplying matrix G_t with P, the projector subtracts the rows of G_t from their weighted average $(e^T W_t G_t)/(e^T W_t e)$. Thus, the product PG_t contains the deviations of the LOS directions with respect to their weighted average. Consequently, $m\sigma_G$ indicates the magnitude of these residuals. The larger the dispersion σ_G or the more the number of satellites m, the smaller the $\bar{\sigma}_{\hat{x}}$ becomes. The second expression of (24) concerns the average precision gain $\mathcal{G}_{\hat{x}}$. It is mainly driven by the code-to-phase standard-deviation ratio $\sigma_p/(\lambda\,\sigma_\phi)$, in which λ is the geometric average of the satellite-specific wavelengths λ_s $(s = 1, \ldots, m)$. By resolving the integer-estimable ambiguities $z = F^T \tilde{a}$, the ambiguity-resolved phase data can contribute to the estimation of x. Therefore, the improvement in precision of $\hat{x}$ is proportional to the ratio $\sigma_p/(\lambda\,\sigma_\phi)$. Next to this ratio, the average precision gain $\mathcal{G}_{\hat{x}}$ is also driven by the parameter ι. According to (25), ι measures the difference between the two weight matrices W_t and $\bar{W}_t$. Their difference is due to the presence of the diagonal matrix $(1/r)R$. As the last rows of Table 1 show, each LEO constellation has satellite-specific frequencies that are relatively close to one another, meaning that the frequency ratios r_s $(s = 1, \ldots, m)$ are very close to their geometric average r. As a result, matrix $(1/r)R$ can be well approximated by the identity matrix I_m, showing $\bar{W}_t \approx W_t$. For existing LEO constellations, the ι-parameter is thus close to one, i.e., $\iota \approx 1$.

The last expression of (24) concerns the ADOP $\bar{\sigma}_{\hat{z}}$. As shown, next to the SD phase standard deviation $\sqrt{2}\,\sigma_\phi$ and number of satellites m, ADOP is also governed by the average precision gain $\mathcal{G}_{\hat{x}}$ and the geometric average of the frequency ratios r_s $(s = 1, \ldots, m)$. When large precision improvement is expected by IAR, i.e., when $\mathcal{G}_{\hat{x}}$ is large, successful IAR becomes challenging in the sense of having large ADOPs (Odijk and Teunissen 2008). The expression also shows that the ADOP $\bar{\sigma}_{\hat{z}}$ is proportional to $r^{\frac{1}{m-1}}$, in which r is the geometric average of the frequency ratios r_s $(s = 1, \ldots, m)$. In the case of GNSS CDMA signals, the ratios are all equal to one, i.e., $r = 1$. However, for the frequency-varying signals such as those of the GLONASS

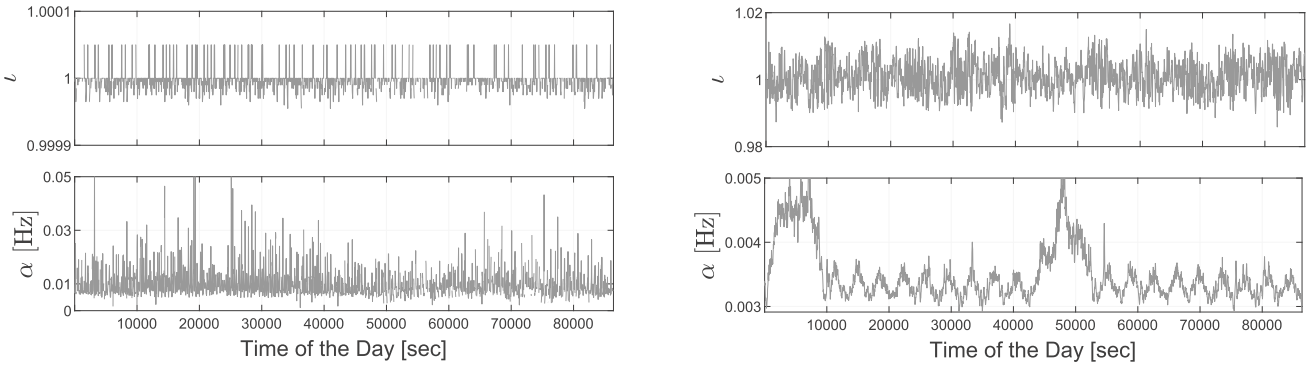

Fig. 5 Values of the ι- (top) and α-parameters (bottom) that are given in (25) and (27), respectively. The results correspond to Iridium (left) and OneWeb (right) satellites (cf. Figure 4)

FDMA or LEO constellations, the ratios (and therefore r) can be significantly larger than one. For instance, the geometric average of the Iridium ratios r_s in (17) is $r \approx 16,262,708$. By tracking 8 Iridium satellites ($m = 8$), we get the relatively large factor $r^{\frac{1}{m-1}} \approx 10.7$ which considerably enlarges the ADOP, making successful single-epoch IAR impossible. To get some numerical insights, consider Fig. 4 showing values of the three performance metrics $\bar{\sigma}_{\hat{x}}$, $\mathcal{G}_{\hat{x}}$, and $\bar{\sigma}_{\hat{z}}$ for the Iridium (left) and OneWeb (right) satellites over a day. If the Iridium and OneWeb satellites would broadcast code measurements as precise as those of GNSS, the PC model is expected to deliver meter- and decimeter-levels float positioning solutions, respectively. That the OneWeb average precision $\bar{\sigma}_{\hat{x}}$ is smaller than its Iridium counterpart is because the number of visible OneWeb satellites is almost twice that of the Iridium satellites.

Now consider the second row of Fig. 4. For both the Iridium and OneWeb cases, we observe large precision gain values. However, the OneWeb average precision gain $\mathcal{G}_{\hat{x}}$ is much larger than its Iridium counterpart. This is because of the much smaller OneWeb wavelength $\lambda \approx 2.5$ [cm] than the Iridium wavelength $\lambda \approx 18.4$ [cm], and the assumption that the precision of the phase data is inversely proportional to their wavelengths (cf. 13). Here we set $\sigma_\phi = 0.01$ [cycle]. As such standard deviation can be optimistic, we will also consider more pessimistic cases in Sect. 5.

Finally, consider the third row of Fig. 4. While the Iridium ADOP varies between 10 and 80 cycles, that of the OneWeb is significantly smaller, being around 0.25 cycles. This seems to be at odds with the larger OneWeb precision gain values. Recall that a large precision gain corresponds to a large ADOP. However, it is the geometric average r which causes such a large discrepancy between the Iridium and OneWeb ADOPs. For the Iridium case, we have $r \approx 16,262,708$. Thanks to the large GCD of the OneWeb frequencies (Table 1), the corresponding geometric average is $r = 467.4$ that is more than four orders of magnitude smaller than that of the Iridium. As a consequence, the larger factor $r^{\frac{1}{m-1}}$ of the Iridium leads to a larger ADOP.

Summarizing the results in Fig. 4, one can conclude that successful IAR would be indeed beneficial for positioning, but seems to be infeasible due to large ADOPs (larger than 0.14 cycles). The results are based on the assumption that precise code data ($\sigma_p = 20$ [cm]) are broadcast by the LEO satellites. In the absence of code data, the dual-epoch P model (14) can be alternative option. Expressions for its performance metrics are presented below.

Lemma 2 (Performance of the P model relative to the PC model) *The average precision $\bar{\sigma}_{\hat{x}}$, precision gain $\mathcal{G}_{\hat{x}}$, and the ADOP $\bar{\sigma}_{\hat{z}}$ of the P model (14) are related to those of the PC model (11) as follows*

$$\begin{aligned} \frac{\bar{\sigma}^{\mathrm{P}}_{\hat{x}}}{\bar{\sigma}^{\mathrm{PC}}_{\hat{x}}} &\approx \frac{\sqrt{2}}{\iota}\,\frac{\lambda\sigma_\phi}{\sigma_p}\,\frac{1}{\alpha\,\Delta t} \\ \frac{\mathcal{G}^{\mathrm{P}}_{\hat{x}}}{\mathcal{G}^{\mathrm{PC}}_{\hat{x}}} &\approx \sqrt{2}\,\frac{\bar{\sigma}^{\mathrm{P}}_{\hat{x}}}{\bar{\sigma}^{\mathrm{PC}}_{\hat{x}}} \\ \frac{\bar{\sigma}^{\mathrm{P}}_{\hat{z}}}{\bar{\sigma}^{\mathrm{PC}}_{\hat{z}}} &\approx \frac{1}{\sqrt{2}}\left(\frac{\mathcal{G}^{\mathrm{P}}_{\hat{x}}}{\mathcal{G}^{\mathrm{PC}}_{\hat{x}}}\right)^{\frac{3}{m-1}} \end{aligned} \tag{26}$$

where

$$\alpha = \left(\frac{\sqrt{|\dot{G}^T\bar{W}\bar{P}\dot{G}|}}{\sqrt{|G^T\bar{W}\bar{P}G|}}\right)^{\frac{1}{3}} \tag{27}$$

with Δt being the sampling interval between the two epochs t and $t+1$. The time-derivative of matrix $G = (1/2)(G_t + G_{t+1})$ is evaluated by $\dot{G} = (G_{t+1} - G_t)/\Delta t$, with $\bar{W} = (1/2)(\bar{W}_t + \bar{W}_{t+1})$.

Proof The proof is given in Appendix A. □

In (24), we have used the superscripts $\cdot^{\mathrm{P}}$ and $\cdot^{\mathrm{PC}}$ to distinguish the performance metrics of the P model from their PC

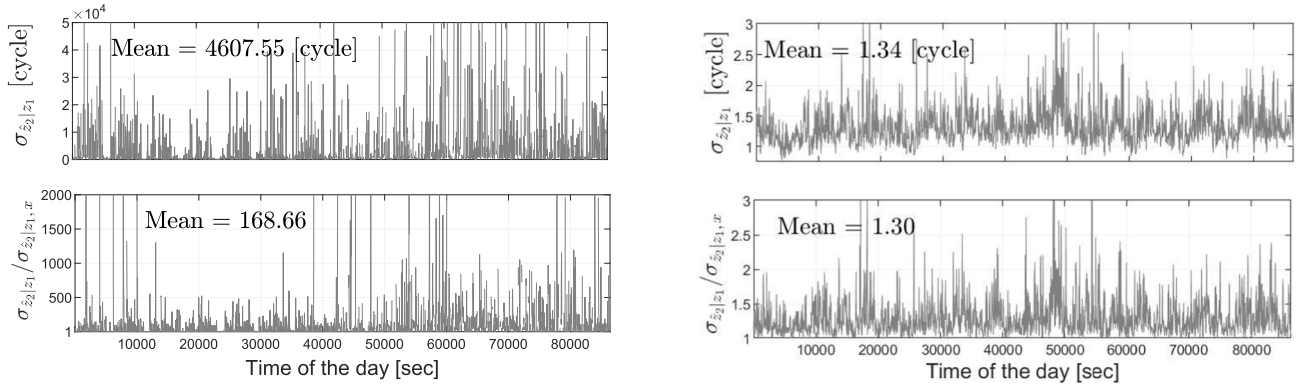

Fig. 6 Values of the conditional standard deviation $\sigma_{\hat{z}_2|z_1}$ (top) and the ratio $\sigma_{\hat{z}_2|z_1}/\sigma_{\hat{z}_2|z_1,x}$ (bottom) given in (28). The results correspond to Iridium (left) and OneWeb (right) satellites (cf. Figure 4). The measurement sampling rate is set to $\Delta t = 1$ s

versions. Given the approximation $\iota \approx 1$, the first expression of (26) shows that 1) the standard deviations of the float position solution $\hat{x}$ are enlarged by a factor of $\sqrt{2}$ because only the between-epoch difference $\Delta\phi_{t+1} - \Delta\phi_t$ contributes to $\hat{x}$, 2) the phase standard deviation $\lambda\sigma_\phi$ replaces its code counterpart σ_p, and 3) the average precision $\bar{\sigma}^{\mathrm{P}}_{\hat{x}}$ is inversely proportional to the dimensionless product $\alpha\,\Delta t$. The longer the measurement sampling interval Δt or the larger the α-parameter, the more precise the float solution $\hat{x}$ becomes. Figure 5 shows values of the ι- (top) and α-parameters (bottom) corresponding to the Iridium (left) and OneWeb (right) satellites over a day (cf. Figure 4). As stated previously, the ι-parameter is close to one for each of the Iridium and OneWeb constellations due to their near-identical satellite-specific wavelengths. However, the α-parameter of the OneWeb satellites is an order of magnitude smaller than its Iridium counterpart. According to (27), α measures the time change $\dot{G}$ relative to the LOS direction vectors in G. It means that the higher the satellite altitude, the slower the time change in the receiver-to-satellite LOS directions, thereby the smaller the parameter α becomes. The smaller values of the OneWeb α is due to the higher altitude of the OneWeb satellites ($\sim$1200 km) than that of the Iridium satellites ($\sim$780 km). For the Iridium case, α is around 0.01 [Hz]. When the measurement sampling interval is $\Delta t = 1$ [sec], setting $\sigma_\phi = 0.01$ [cycles] and $\sigma_p = 20$ [cm] gives $\bar{\sigma}^{\mathrm{P}}_{\hat{x}} \approx 1.3\,\bar{\sigma}^{\mathrm{PC}}_{\hat{x}}$. Therefore, for the case of Iridium, the dual-epoch P model delivers slightly less precise float position solutions $\hat{x}$ than the single-epoch PC model does. With reference to Fig. 4, meter-level float position solutions are also expected by the P model.

According to the second expression of (26), the relative gain ratio $\mathcal{G}^{\mathrm{P}}_{\hat{x}}/\mathcal{G}^{\mathrm{PC}}_{\hat{x}}$ is equal to the precision ratio $\bar{\sigma}^{\mathrm{P}}_{\hat{x}}/\bar{\sigma}^{\mathrm{PC}}_{\hat{x}}$ times $\sqrt{2}$. For the Iridium $\alpha \approx 0.01$ [Hz], one can likewise obtain $\mathcal{G}^{\mathrm{P}}_{\hat{x}} \approx 1.8\,\mathcal{G}^{\mathrm{PC}}_{\hat{x}}$. As with the single-epoch PC model, successful IAR is thus beneficial for positioning via the dual-epoch P model. However, as the last expression of (26) implies, the ADOP of the P-model $\bar{\sigma}^{\mathrm{P}}_{\hat{z}}$ can also be as large as $\bar{\sigma}^{\mathrm{PC}}_{\hat{z}}$. The conclusion is that successful IAR is also infeasible under the dual-epoch P model.

3.5 Switching to partial ambiguity-fixing

The results in Figs. 4 and 5 show that *not* all the entries of the float ambiguity vector $\hat{z} = F^T\hat{a}$ can be reliably mapped to their correct integers. An alternative option is to integer-resolve only a subset of the integer-estimable ambiguities whose corresponding success-rate is sufficiently large to ensure reliable ambiguity-fixing. Accordingly, certain combinations of $\hat{z}$ that are poorly precise are excluded from IAR. Applications of such *partial* IAR strategy can be found in, e.g., (Teunissen et al. 1999; Brack 2017; Psychas et al. 2020). As a consequence of this practice, one may achieve a smaller ADOP at the expense of a smaller precision gain for the position solution. In the following, we quantify this when one component of float ambiguity vector $\hat{z}$, say the scalar $\hat{z}_2 = \tilde{l}^T\hat{z}$ ($\tilde{l} \in \mathbb{Z}^{(m-1)}$), is not fixed.

Lemma 3 (Performance of partial IAR) *Let the inverse of the admissible ambiguity matrix* $[\tilde{L}, \tilde{l}]$, *with* $\tilde{L} \in \mathbb{Z}^{(m-1)\times(m-2)}$ *and* $\tilde{l} \in \mathbb{Z}^{(m-1)}$, *be given by* $[L, l]^T$, *i.e.,* $\tilde{L}L^T + \tilde{l}\,l^T = I_{m-1}$. *Also consider a partial IAR strategy in which only the subvector* $\hat{z}_1 = \tilde{L}^T\hat{z}$ *of the float ambiguity vector* $\hat{z}$ *is fixed, while the scalar* $\hat{z}_2 = \tilde{l}^T\hat{z}$ *remains float. The performance metrics of such partial IAR (PAR) are related to those of full IAR (FAR) as follows*

$$\begin{aligned} \mathcal{G}^{\mathrm{PAR}}_{\hat{x}} &= \mathcal{G}^{\mathrm{FAR}}_{\hat{x}} \left(\frac{\sigma_{\hat{z}_2|z_1,x}}{\sigma_{\hat{z}_2|z_1}}\right)^{\frac{1}{3}} \\ \bar{\sigma}_{\hat{z}_1} &= \bar{\sigma}^{\frac{m-1}{m-2}}_{\hat{z}} \left(\frac{1}{\sigma_{\hat{z}_2|z_1}}\right)^{\frac{1}{m-2}} \end{aligned} \tag{28}$$

in which the conditional standard deviations are given by $\sigma_{\hat{z}_2|z_1} = 1/\sqrt{l^T Q_{\hat{z}\hat{z}}^{-1} l}$ *and* $\sigma_{\hat{z}_2|z_1,x} = 1/\sqrt{l^T Q_{\hat{z}\hat{z}|x}^{-1} l}$, *where* $Q_{\hat{z}\hat{z}|x} = Q_{\hat{z}\hat{z}} - Q_{\hat{z}\hat{x}} Q_{\hat{x}\hat{x}}^{-1} Q_{\hat{x}\hat{z}}$.

Proof The proof is given in Appendix A. □

The first expression of (28) establishes a link between the average precision gain $\mathcal{G}_{\hat{x}}^{\mathrm{PAR}}$ and its version $\mathcal{G}_{\hat{x}}^{\mathrm{FAR}}$ obtained by full IAR. The second expression links the partial ADOP $\bar{\sigma}_{\hat{z}_1}$ to its version $\bar{\sigma}_{\hat{z}}$ obtained by full IAR. Since the scalar $\hat{z}_2$ never gets less precise by imposing the extra constraint $\hat{x} = x$, the conditional standard deviation $\sigma_{\hat{z}_2|z_1,x}$ is never larger than $\sigma_{\hat{z}_2|z_1}$. Thus

$$\mathcal{G}_{\hat{x}}^{\mathrm{PAR}} \leq \mathcal{G}_{\hat{x}}^{\mathrm{FAR}}, \tag{29}$$

meaning that smaller precision improvement is experienced by the position solution $\hat{x}$ when switching from full IAR to a partial IAR strategy. Whether one can improve the IAR performance—in the sense of having the partial ADOP $\bar{\sigma}_{\hat{z}_1}$ smaller than $\bar{\sigma}_{\hat{z}}$—depends on the precision of $\hat{z}_2$ when the remaining ambiguities $\hat{z}_1$ have been fixed. The larger the standard deviation $\sigma_{\hat{z}_2|z_1}$, the smaller the partial ADOP $\bar{\sigma}_{\hat{z}_1}$ becomes, thereby the better the IAR performance becomes. Figure 6 presents values of $\sigma_{\hat{z}_2|z_1}$ (top) and the ratio $\sigma_{\hat{z}_2|z_1}/\sigma_{\hat{z}_2|z_1,x}$ (bottom) corresponding to the Iridium (left) and OneWeb (right) satellites over a day (cf. Figure 4). For the Iridium, we have $\sigma_{\hat{z}_2|z_1} \approx 4600$ cycles. Therefore, when tracking 8 Iridium satellites ($m = 8$), the partial ADOP $\bar{\sigma}_{\hat{z}_1}$ is almost 4 times smaller than its full version. The price to pay for such a considerable reduction in ADOP is to experience much smaller precision gain. As the second row of Fig. 6 indicates, the standard deviation $\sigma_{\hat{z}_2|z_1,x}$ on average 170 times smaller than $\sigma_{\hat{z}_2|z_1}$, showing that $\mathcal{G}_{\hat{x}}^{\mathrm{PAR}}$ is much smaller than $\mathcal{G}_{\hat{x}}^{\mathrm{FAR}}$. On the contrary, the corresponding results of OneWeb show that $\sigma_{\hat{z}_2|z_1,x} \approx \sigma_{\hat{z}_2|z_1}$, meaning that average precision gain does not get smaller by much upon switching to partial IAR. The rather small OneWeb standard deviation $\sigma_{\hat{z}_2|z_1}$ also indicates that the reduction in ADOP may not be considerable. As each LEO constellation has a distinct response to partial IAR, in the next section, we consider a simulation platform to study the performance of the dual-epoch P model for several standalone and combined LEO constellations in which a partial IAR strategy is employed.

4 Simulation platform

In this section, we discuss a simulation platform for the positioning experiments of communication LEO satellites with frequency-varying carrier phase measurements. The platform operates in two stages, as illustrated in Fig. 7. First, time-constant and time-varying parameters and dual-epoch carrier phase measurements are generated and registered as reference values. Second, the estimable forms of the parameters are recursively estimated based on the phase-only model and then compared to the reference values.

As discussed in Sect. 2, we make the assumption that the baselines are sufficiently short (e.g., 5 km in the simulation experiments) with high-grade satellite clocks. This allows us to simplify the generation of parameters, together with neglecting between-receiver SD atmospheric delays. We neglect tidal loading, phase center offsets (PCO), phase center variations (PCV), and satellite attitudes, as these factors typically cancel out over short baselines. Additionally, we disregard the clock corrections of LEO satellites, assuming the utilization of high-grade clocks. We also do not consider phase wind-up and multipath effects. Other parameters are simulated as follows:

- **Receiver location.** International GNSS Service (IGS) stations with known precise positions are used as base receivers x_b. A 5-km distance is then added to the time-constant base receiver coordinates to determine the rover receiver locations x_r, thereby forming a simulated baseline.
- **Receiver clock offset.** To satisfy the assumption in Sect. 2 that the receivers are equipped with high-grade clocks, we generate between-receiver SD receiver clock offsets according to $|dt_t| \leq 10^{-7}$ s for both two epochs.
- **Carrier phase ambiguity.** The ambiguity parameter (*in cycle*) for every receiver-satellite pair is a randomly generated integer, created using the MATLAB built-in function `randi.m` and remains constant over time.

After completing the simulation of the true versions of the parameters, one needs to construct the carrier phase measurements. In doing so, the noise for the UD carrier phase measurements ϕ_t^s is modeled as Gaussian with zero mean and a standard deviation of σ_{ϕ^s} (in *cycle*), and the standard deviations are assumed to be *uncorrelated* over time. Consequently, the noise for dual-epoch phase measurements can be generated using the MATLAB built-in function `mvnrnd.m`. The measurement noise for each receiver-satellite pair is specifically simulated as follows:

- **Carrier phase measurement noise.** The zenith-referenced standard deviation of the UD carrier phase measurement σ_{ϕ^s} is simulated to be proportional to the underlying wavelength λ_s, i.e., $\sigma_{\phi^s} = \sigma_\phi \lambda_s$. In the simulation, we set σ_ϕ to 1/100, 1/80, 1/60, 1/40 and 1/20 cycles. Considering the relationship between observation precision and the corresponding elevation angle, the measurement noise along LOS direction for each receiver-satellite pair is inversely proportional to the cosecant of the elevation angle.

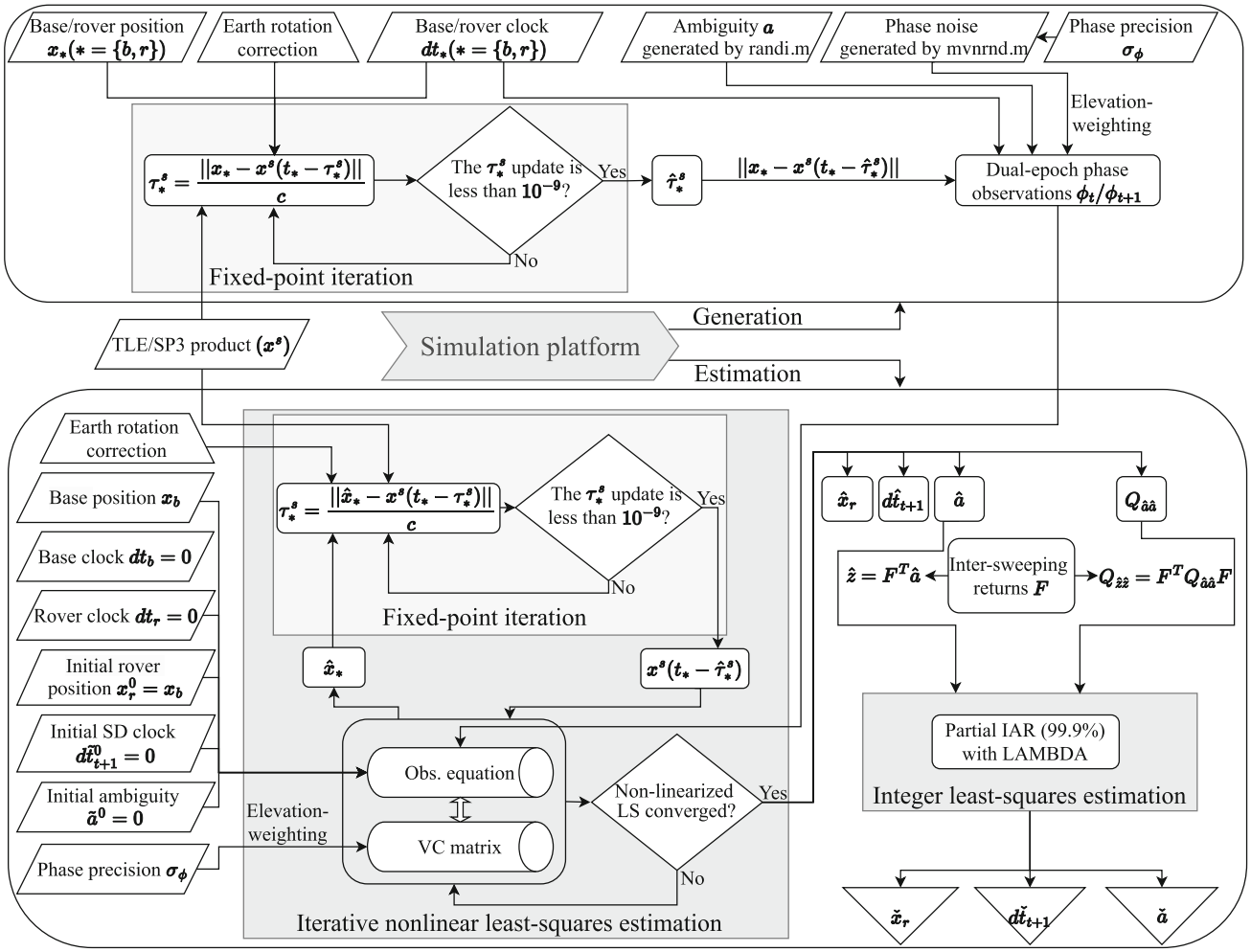

Fig. 7 Simulation platform (in MATLAB) for short-baseline positioning experiments that provides full control over the generation of parameters and measurements, followed by the estimation of estimable parameters

The Keplerian elements of communication LEO satellites are tracked, updated once daily, and made publicly available by the North American Aerospace Defense Command (NORAD) in the format of Two-Line Element (TLE) files (https://celestrak.org/NORAD/elements/). Using these elements, one can evaluate the position of the required satellite x^s with the Simplified General Perturbations model 4 (SGP4) (Vallado and Crawford 2008). With the previously simulated UD receiver clock offset, the signal reception time t_r^s (or t_b^s) can be determined at the predefined sampling time. Given the true receiver location x_r (or x_b) as earlier simulated, satellite position x^s accounting for Earth rotation correction and the signal reception time t_r^s (or t_b^s), the true receiver-to-satellite distance $||x_r - x^s(t_r^s - \tau_r^s)||$ (or $||x_b - x^s(t_b^s - \tau_b^s)||$) is computed, where the signal travel time τ_r^s (or τ_b^s) is recursively estimated according to the Fixed-Point algorithm (de Jonge 1998, Chapter 2), then combined with the UD receiver clock offset and carrier phase ambiguity. Finally, lumped with the elevation-dependent measurement noise, the simulated carrier phase measurement for each receiver-satellite pair is obtained.

In the estimation process, the LEO satellite orbits x^s are also obtained from the TLE files. The base receiver's location is assumed to be known, while the rover receiver's position needs to be estimated with the coordinate of the base receiver used as the initial value. In the situation where both the base and rover receivers have no access to code measurements, one can only rely on carrier phase measurements to enable linearization and recursively compute the corresponding signal travel time $\hat{\tau}_r^s$ (or $\hat{\tau}_b^s$) also based on the Fixed-point algorithm, accounting for Earth rotation corrections. Then, we employ the dual-epoch phase-only model (14) with the elevation-dependent joint variance matrix to obtain ambiguity-float solutions (receiver position $\hat{x}_r$, estimable SD clock offset $d\hat{t}_t$ and estimable ambiguities $\hat{a}$) by employing the minimum-variance least-squares estimation. To obtain the integer-estimable combinations of the ambiguities, the integer-sweeping algorithm is utilized

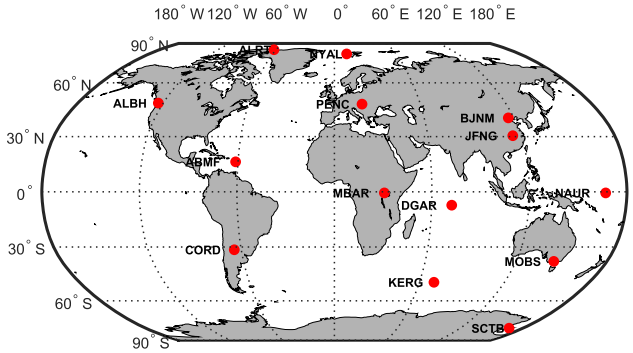

Fig. 8 Distribution of the 14 IGS stations (red dots) as utilized in the simulation study

to generate the integer matrix F. Subsequently, the integer-estimable float ambiguity solution $\hat{z} = F^T \hat{a}$ and its variance matrix $Q_{\hat{z}\hat{z}} = F^T Q_{\hat{a}\hat{a}} F$ are calculated. Using them as inputs, and following the application of partial IAR with a minimum required integer least-squares (ILS) success-rate of 99.9%, ambiguity-fixed solutions (receiver position $\check{x}_r$, estimable SD clock offset $d\check{t}_t$ and estimable ambiguities $\check{a}$) can be obtained. To evaluate the corresponding ILS ambiguity success-rates, we employ the Ps-LAMBDA software (Verhagen et al. 2013).

5 Dual-epoch phase-only model at work

As analyzed in Sect. 3, each LEO constellation responds distinctly to partial IAR depending on various factors, such as sampling interval Δt, number of satellites m and precision of carrier phase measurements σ_ϕ. To investigate whether it is feasible to achieve partial IAR and under what circumstances partial IAR can benefit positioning solutions, 14 globally distributed IGS stations, shown in Fig. 8, are used for the simulation experiments of dual-epoch phase-only positioning. Each station (red dot) in the figure serves as base receiver supporting a rover receiver whose inter-station distance is about 5 km. In doing so, we analyze the empirical accuracy of positioning errors for different Δt, m, and σ_ϕ. To illustrate the impact of the SD receiver clock dt_t on both the IAR and positioning performance, various bias-magnitude of dt_t is also considered. Particularly, we consider multi-LEO and GNSS-augmented LEO positioning in *mid- to low-latitude* regions and *signal-obstructed* areas where the number of available satellites for a single LEO constellation are limited. The data processing strategies for the LEO dataset and parameter configurations are presented in Table 2. For each positioning simulation, we perform 10,000 repetitions using normally distributed carrier phase measurements with a standard deviation σ_ϕ. Subsequently, we evaluate the root-mean-squared (RMS) error of the corresponding positioning results as a measure of the empirical accuracy.

5.1 Impacts of the number of satellites on positioning

We first consider the Iridium-only results with the sampling interval $\Delta t = 30$ s. The shorter sampling interval $\Delta t = 1$ s can only deliver meter-level float positioning solutions, while none of its float ambiguities are precise enough to meet the minimum required success-rate of 99.9%. In contrast, increasing Δt to 30 s enhances the precision of ambiguity-float positions (cf. the first expression in 26) and potentially enables partial IAR (cf. the third expression in 26). However, the third expression suggests that a sufficiently large number of satellites m is required to lower the ADOP to a level where partial IAR becomes achievable, which motivates our investigation into the impacts of the number of satellites on partial-fixed positioning using the dual-epoch phase-only model (14) with $\Delta t = 30$ s. As an illustrative example, we display the results of a 5-km baseline conducted at station NYAL at a cut-off elevation angle of 5° shown in Fig. 9, presenting RMSs of ambiguity-float positioning solutions (left), along with the corresponding float-to-fixed RMS ratios and fixed-to-all ambiguity number ratios (right) after applying partial IAR with a minimum required ILS success-rate of 99.9%. These metrics are plotted as a function of the number of Iridium satellites m for varying levels of carrier phase measurement precision σ_ϕ.

With an optimistic carrier phase measurement precision of $\sigma_\phi = 1/100$ cycles, at least 5 Iridium satellites are required to achieve ambiguity-float positioning accuracy of less than 0.5 m in all three directions. A minimum of 6 Iridium satellites is necessary to successfully achieve partial IAR. With a fixed-to-all ambiguity number ratio of about 20% at this stage, the improvement in partial-fixed positions compared to the float counterparts is approximately twofold in the east direction, while minimal improvements are observed in the north and up directions. As the number of Iridium satellites increases, the ambiguity-float positioning accuracy improves, and the float-to-fixed RMS ratio increases in all three directions, along with an increase in the fixed-to-all ambiguity number ratio. Using the maximum available 11 Iridium satellites, centimeter-level partial-fixed positioning can be achieved, with float-to-fixed RMS ratios of approximately 3, 7, and 3 in the north, east, and up directions, respectively.

If the carrier phase measurements are less precise, e.g. $\sigma_\phi = 1/60$ cycles, centimeter- to decimeter-level ambiguity-float positioning can be achieved as the number of Iridium satellites m increases from 5 to 11. With at least 8 to 10 satellites, the fixed-to-all ambiguity number ratio remains below 50%, and there is no significant enhancement in partial-fixed position solutions compared to the float versions. To successfully achieve partial IAR with a fixed-to-all ambiguity number ratio greater than 50%, at least 11 satellites are required, with the corresponding float-to-fixed RMS ratios

Table 2 Strategies for simulated short-baseline positioning experiments

LEO data	
Baseline length	5 km
Date	December 19, 2023
Epoch time	01:30 GPS time (two epochs)
Number of satellites m	Minimum of 4
Sampling interval Δt	1 s, 30 s
Cut-off elevation	5°, 10°, 15°, 20°, 25°, 50°
Frequencies	Shown in Table 1
Precise satellite corrections	
Satellite clocks dt^s	GPS-grade
Satellite orbits x^s	TLE files (assumed to be precise)
Linearization	
Initial rover receiver's position	Base receiver's location x_b
SD receiver clock offset	$\lvert dt_t \rvert \leq 10^{-7}$ s
Estimated parameters	
Rover receiver position	Time-constant
Estimable receiver clock offsets	Unlinked in time
Estimable phase ambiguities	Time-constant
Stochastic model	
Phase zenith-referenced precision σ_ϕ	1/100, 1/80, 1/60, 1/40, 1/20 [cycles]
Weighting model	Cosecant elevation function
Estimation strategy	
Positioning model	Dual-epoch phase-only (14)
Estimation principle	Minimum variance least-squares estimation
Ambiguity resolution	
Estimation principle	Integer least squares (ILS)
IAR method	Partial IAR (99.9%) with LAMBDA

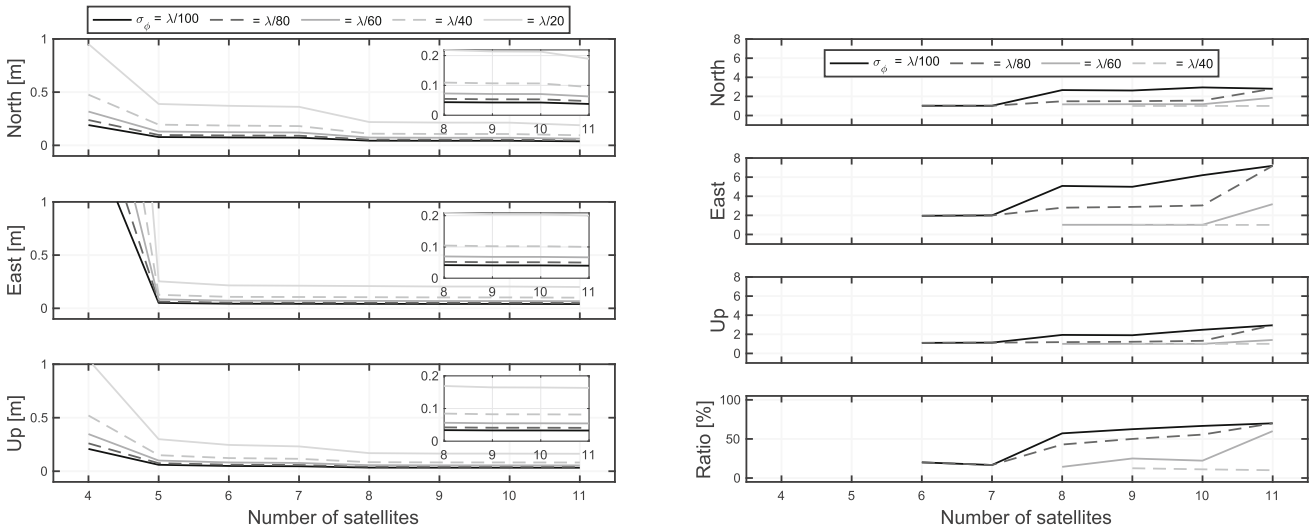

Fig. 9 RMSs (m) of ambiguity-float positioning solutions (left), and the corresponding float-to-fixed RMS ratios and fixed-to-all ambiguity number ratios (%) after partial IAR with a minimum required ILS success-rate of 99.9% (right) as a function of the number of Iridium satellites m for different carrier phase measurement precision σ_ϕ, based on the dual-epoch phase-only model (14) with a 30-s sampling interval Δt for the 5-km baseline located in station NYAL at a cut-off elevation angle of 5°. For simplicity, only the simulation results at 5400 s on December 19, 2023 are presented. Note, for $\sigma_\phi = 1/20$ cycles, the minimum success-rate requirement is not met. Thus, the corresponding fixed results are absent

being approximately 2, 3 and 2 in the north, east, and up directions, respectively.

For even lower carrier phase measurement precision $\sigma_\phi = 1/40$ cycles, there is no significant improvement in positioning accuracy for partial IAR with a fixed-to-all ambiguity number ratio of about 10%, even with the maximum number of observable Iridium satellites. In this case, the ambiguity-float positioning solution has a RMS of approximately 0.1 m in all three directions.

The Iridium 5-km baseline positioning based on (14) with $\Delta t = 1$ s can only deliver meter-level ambiguity-float positioning solutions. This is in agreement with the earlier results shown in Fig. 4.

This is, however, not the case with the OneWeb results. It is feasible to improve the precision of the results when $\Delta t = 1$ s. With sufficient number of satellites, up to 34, the OneWeb-only constellation for $\Delta t = 1$ s achieves decimeter-level accuracy of ambiguity-float solutions in all three directions for $\sigma_\phi = 1/60$ cycles shown on the left panel of Fig. 10. As depicted on the right panel of the figure, it can successfully achieve partial IAR when the number of satellites exceeds 22, with fixed-to-all ambiguity number ratios higher than about 90%. In this case, partial IAR achieves float-to-fixed RMS ratios of approximately 330, 1260 and 270 in the north, east and up directions, respectively.

5.2 Empirical analysis of position errors across various receiver clock quality levels

In the absence of code data, the estimable receiver clock offset is biased by the carrier phase ambiguity of the pivot satellite and thus cannot be used for the linearization of the observation equations. As a result, we are forced to assume that the clock offsets for each receiver are zero, which increases the risk of incorrect linearization and negatively impacts the overall positioning performance. In this sub-section, we investigate the effects of receiver clocks of varying qualities on partial IAR performance for Iridium-only satellites. The results of 5-km baseline positioning for the NYAL station are also presented as an illustrative example. The number of Iridium satellites and cut-off elevation angle are set to 11 and 5°, respectively.

As the between-receiver SD receiver clock offset dt_t increases, the empirical RMSs of both ambiguity-float and partial-fixed solutions become large, as shown in Fig. 11, which presents RMSs of ambiguity-float positioning solutions, and the corresponding float-to-fixed RMS ratios, success-rates ('SR') and fixed-to-all ambiguity number ratios ('Ratio') after applying partial IAR with a minimum required success-rate of 99.9% as a function of SD clock offset dt_t for different carrier phase measurement precision σ_ϕ, based on the dual-epoch phase-only model (14) with a 30-s sampling interval Δt.

Specifically, with an optimistic σ_ϕ of 1/100 cycles, the RMSs of ambiguity-float position errors are approximately 4 cm, 4 cm and 3 cm in the north, east and up directions, respectively, when the offset dt_t is small (e.g., 0.01 microseconds). As the offset increases, the RMSs grow, particularly in the east direction, reaching about 6 cm, 41 cm and 5 cm, respectively, when the offset reaches 100 microseconds. Note that the noise of the dual-epoch phase-only equations (14) before fixing ambiguities is larger than after ambiguity resolution. Thus, our previous assumption that the SD clock offset dt_t is less than 0.1 microseconds can be relaxed for ambiguity-float solutions. This explains why the ambiguity-float position errors are not significantly affected by dt_t as long as it remains below approximately 10 microseconds.

In terms of partial-fixed positions, the float-to-fixed RMS ratios are about 9.8, 11.9 and 3.3 in the north, east and up directions, respectively, with 100% success-rates and 80% fixed-to-all ambiguity number ratios before the SD clock offset dt_t reaches 0.1 microseconds. Beyond this point, the float-to-fixed RMS ratios decrease sharply, although success-rates and fixed-to-all ambiguity number ratios remain at 100% and 80%, respectively, until the offset reaches 1 microsecond. When dt_t exceeds 1 microsecond, both success-rates and fixed-to-all ambiguity number ratios begin to decline significantly. At an offset of 4 microseconds, with success-rates of 25% and fixed-to-all ambiguity number ratios of 20%, improvements in position accuracy are observed only in the horizontal directions, with float-to-fixed RMS ratios of approximately 7.2 in the north direction and 1.3 in the east direction. For offsets larger than 5 microseconds, improvements are achieved only in the north direction, with float-to-fixed RMS ratios greater than approximately 6.7, while the other directions experience degradation to values below 1. This trend continues until the offset exceeds 6 microseconds, at which point float-to-fixed RMS ratios in all three directions all drop below 1. This empirically verifies our previous assumption that receivers are equipped with high-grade clocks, ensuring that the SD clock offset is less than 0.1 microseconds to neglect the bias vector ε_t in (4), which potentially enables the achievement of partial IAR. If the SD clock offset becomes larger however, there is a risk of incorrectly fixed ambiguities and increased positioning errors.

5.3 Performance of multi-LEO/GNSS positioning in Iridium-challenged environments

As listed in Table 1, the near-polar orbits of the Iridium constellation provide dense satellite coverage at high latitudes, while in *mid- to low-latitude* regions, tracking a sufficient number of Iridium satellites becomes challenging. Additionally, despite the Iridium constellation currently consisting of 75 active satellites, it can be difficult to observe mea-

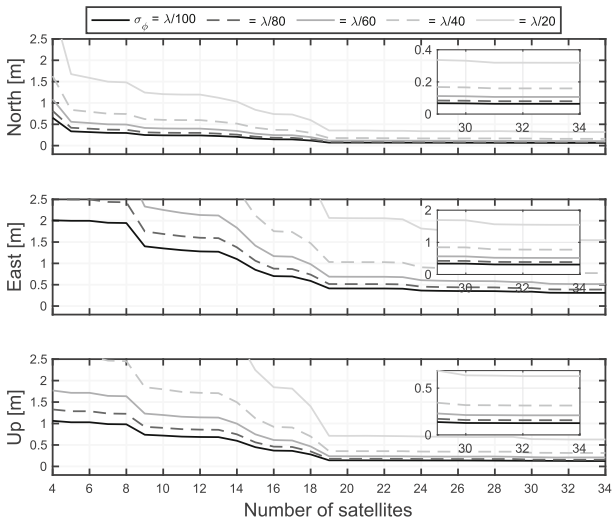

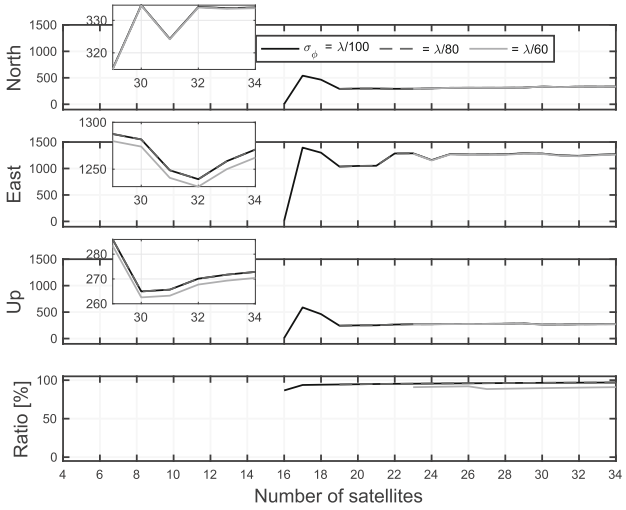

Fig. 10 RMSs (m) of ambiguity-float positioning solutions (left), and the corresponding float-to-fixed RMS ratios and fixed-to-all ambiguity number ratios (%) after partial IAR with a minimum required ILS success-rate of 99.9% (right) as a function of the number of OneWeb satellites m for different carrier phase measurement precision σ_ϕ, based on the dual-epoch phase-only model (14) with a 1-s sampling interval Δt for the 5-km baseline located in station BJNM at a cut-off elevation angle of 5°. For simplicity, only the simulation results at 5400 s on December 19, 2023 are presented. Note, for $\sigma_\phi = 1/20$ and $1/40$ cycles, the minimum success-rate requirement is not met. Thus, the corresponding fixed results are absent

surements from the Iridium-only constellation that meet the minimum required quantity in severely *signal-obstructed* environments due to its orbital altitude of about 780 km. For the former scenario, we therefore compare the positioning performance of GNSS-assisted Iridium/Globalstar constellations operating in the L-band in mid- to low-latitude regions against multi-Iridium/Globalstar positioning, using 14 globally distributed baselines shown in Fig. 8. For the latter scenario, we first investigate the impact of cut-off elevations on single-LEO constellation (Iridium-only) positioning, then discuss an extreme cut-off case where city canyons cause significant signal obstruction by buildings. In this case, only measurements transmitted by multi-LEO/GNSS satellites at a high cut-off elevation, e.g., 50°, can be received.

Based on the dual-epoch phase-only model (14) with a 30-s sampling interval Δt, only the ALRT and NYAL stations, situated in high-latitude regions with over 10 multi-Iridium/Globalstar satellites at a cut-off elevation of 5°, achieve centimeter-level RMS of ambiguity-float positioning errors in all three directions for $\sigma_\phi = 1/80$ cycles as shown in the left sub-figure in Fig. 12. At the ALRT station, which has 11 Iridium satellites (no Globalstar satellites), the RMSs of partial-fixed positioning errors are approximately 9 mm, 19 mm and 18 mm in the north, east and up directions, respectively, showing improvements of about 64%, 23% and 49% compared to the float counterparts. For the NYAL station, which has 11 Iridium and 1 Globalstar satellites, the RMSs are approximately 17 mm, 7 mm and 14 mm, achieving improvements of about 64%, 86% and 66% in the north, east and up directions, respectively. To strengthen the credibility of the analysis, we also present the positioning performance of the NYAL station over one day (see Fig. 13). Consistent with the results at our sampled epoch, the accuracy improvements over the day suggest the benefits of partial IAR on multi-Iridium/Globalstar-based positioning. The remaining stations are located in mid- to low-latitude regions, where the number of multi-Iridium/Globalstar satellites observed at a cut-off elevation of 5° ranges from 2 to 7, achieving a 3-dimensional ambiguity-float positioning accuracy at decimeter to meter levels. However, these stations are unable to achieve the minimum required success-rate for partial IAR due to the insufficient number of satellites. To address this, we use the GNSS constellations (i.e., GPS/GLONASS/Galileo) to assist the Iridium/Globalstar constellations. As shown in the right sub-figure in Fig. 12, with more than 25 satellites available, all stations in mid- to low-latitude regions also achieve meter-level ambiguity-float positioning accuracy. More importantly, they can successfully achieve partial IAR and obtain millimeter-level positioning accuracy in all three directions, demonstrating the benefits of GNSS assistance for communication LEO positioning in mid- to low-latitude regions.

In complex urban environments, such as city canyons where signals are easily obstructed by buildings, one can only use those measurements transmitted by satellites at a high cut-off elevation. To ensure sufficient satellite coverage at such high cut-off, we expand our analysis to include multi-LEO/GNSS constellations and investigate their positioning

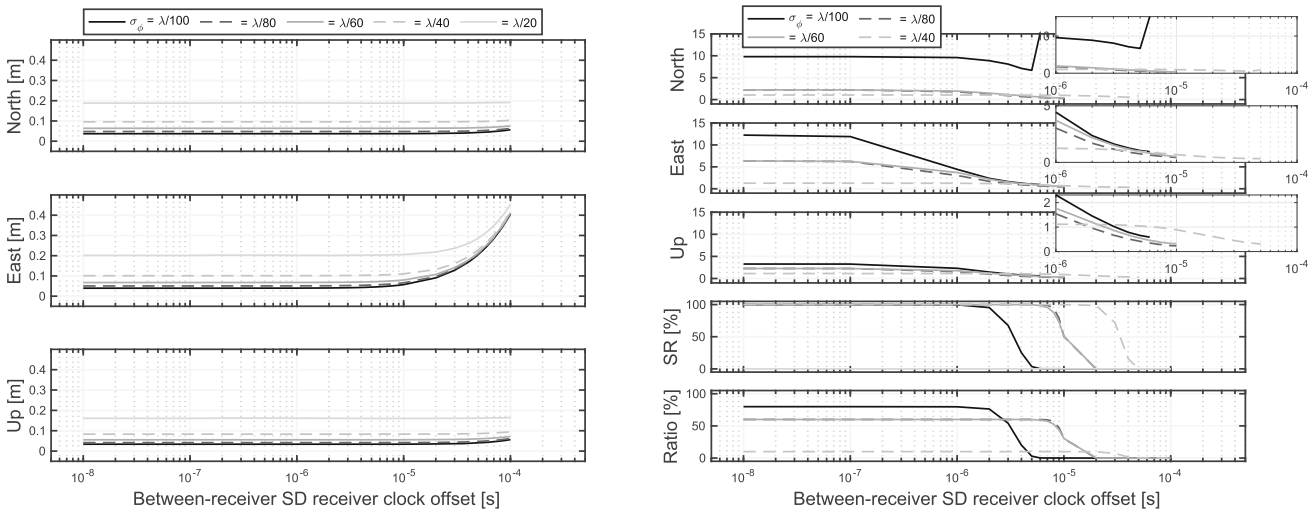

Fig. 11 RMSs (m) of ambiguity-float positioning solutions (left), and the corresponding float-to-fixed RMS ratios, success-rates ('SR', %) and fixed-to-all ambiguity number ratios ('Ratio', %) after partial IAR with a minimum required ILS success-rate of 99.9% (right) as a function of the between-receiver SD receiver clock offset dt_t for different carrier phase measurement precision σ_ϕ, based on the dual-epoch phase-only model (14) with a 30-s sampling interval Δt for the 5-km baseline located in station NYAL, observing 11 Iridium satellites at a cut-off elevation angle of 5°. For simplicity, only the simulation results at 5400 s on December 19, 2023 are presented. Note, for $\sigma_\phi = 1/20$ cycles, the minimum success-rate requirement is not met. Thus, the corresponding fixed results are absent

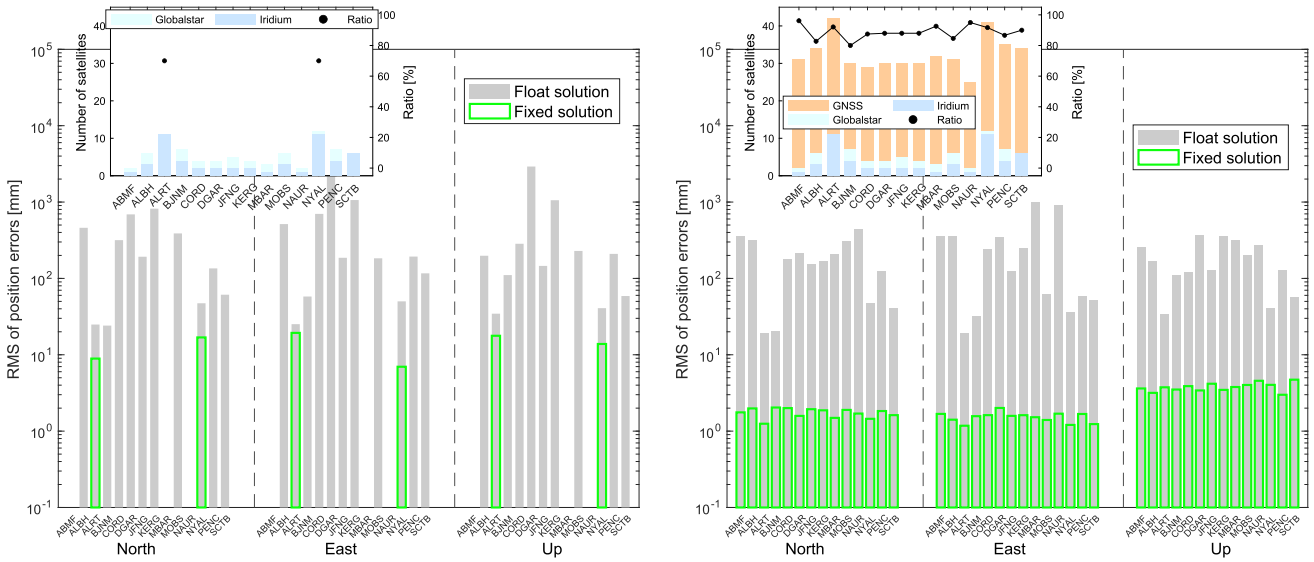

Fig. 12 RMSs (mm) of ambiguity-float positioning errors (gray bar charts) and their fixed versions (green boxes) after partial IAR with a minimum required ILS success-rate of 99.9%, based on the dual-epoch phase-only model (14) with a 30-s sampling interval Δt at a cut-off elevation angle of 5° for 14 IGS stations, where the carrier phase measurement precision σ_ϕ is 1/80 cycles. The top-left inset in each figure illustrates the available satellite numbers of each constellation (vertical bar charts with different colors) and the fixed-to-all ambiguity number ratios (black lines) for the 14 stations. The left and right sub-figures are the results of multi-Iridium/Globalstar and multi-Iridium/Globalstar/GNSS, respectively, where GNSS includes frequency-identical GPS/Galileo and frequency-varying GLONASS signals. For simplicity, only the simulation results at 5400 s on December 19, 2023, are presented

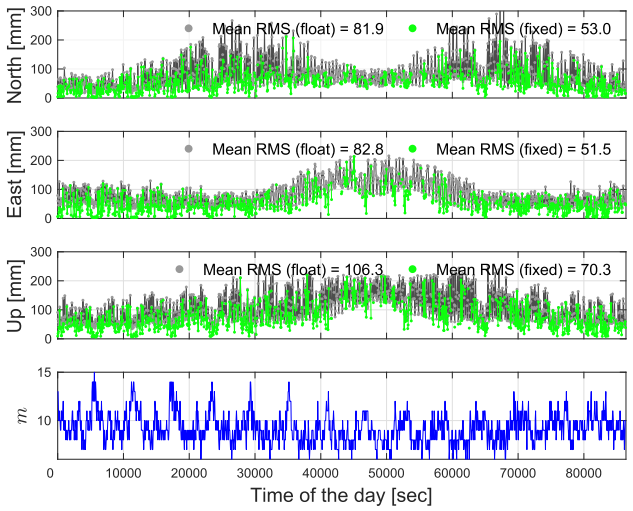

Fig. 13 Time-series of RMSs (mm) of ambiguity-float positioning errors (gray lines) and their fixed versions (green lines) after partial IAR with a minimum required ILS success-rate of 99.9% over one day (19 of December of 2023), based on the dual-epoch phase-only model (14) with a 30-s sampling interval Δt for the 5-km baseline located in station NYAL, observing multi-Iridium/Globalstar satellites at a cut-off elevation angle of 5°, where the carrier-phase measurement precision σ_ϕ is 1/80 cycles

performance. To guarantee adequate satellite availability, the following experiments include three mature GNSS constellations: GPS, GLONASS and Galileo, as well as five common communication LEO constellations: Iridium, Globalstar, Starlink, OneWeb and Orbcomm. It is noteworthy that, unlike the Iridium constellation, whose signals span the L-band, the Starlink and OneWeb constellations operate in the Ku-band. Consequently, according to empirical values of the L-band GNSS systems that the precision of carrier phase measurements is approximately one hundredth of the corresponding wavelength, the precision of Starlink and OneWeb carrier phase measurements can reach the sub-millimeter level, which is highly ideal. As such, we assess the positioning capabilities of the multi-LEO/GNSS constellations, assuming a more realistic precision of $\sigma_\phi = 1/40$ cycles.

Before that, we first need to investigate how cut-off elevations impact positioning with a single LEO constellation (e.g., Iridium-only) to determine under what conditions combining multi-LEO/GNSS constellations is necessary. The results of 5-km baseline positioning for the NYAL station are also presented as an example.

As shown in Fig. 14, which presents the RMSs of ambiguity-float positioning solutions (left) and the corresponding float-to-fixed RMS ratios and fixed-to-all ambiguity number ratios (right) as a function of the cut-off elevation for different carrier phase measurement precision σ_ϕ, increasing the sampling interval Δt from 1 s to 30 s enhances the accuracy of ambiguity-float positions to the centimeter to decimeter levels and makes partial IAR possible for the Iridium-only constellation in some cases. Specifically, when the cut-off elevation is below 20°, a more pessimistic carrier phase measurement precision of 1/20 and 1/40 cycles achieves ambiguity-float positions of about 0.2 m and 0.1 m in all three directions. Conversely, a more optimistic measurement precision of 1/100, 1/80, and 1/60 cycles results in ambiguity-float positioning accuracy below 0.1 m. Partial IAR is successfully achieved for $\sigma_\phi = 1/100$, 1/80, 1/60 and 1/40 cycles. However, for $\sigma_\phi = 1/40$ cycles, the float-to-fixed RMS ratios are close to 1 in all three directions because the corresponding fixed-to-all ambiguity number ratio is about 10%, regardless of whether the cut-off elevation is 5° or 20°. With higher σ_ϕ, such as 1/60 cycles, float-to-fixed RMS ratios of 2, 3, and 1.5 are achieved at 5° in the north, east, and up directions, respectively. For $\sigma_\phi = 1/80$ and 1/100 cycles, these ratios are 3, 7, and 3, respectively. As the cut-off elevation increases to 25°, achieving partial IAR becomes possible only for $\sigma_\phi = 1/100$ cycles, showing an improvement only in the east direction with a fixed-to-all ambiguity number ratio of about 20%. Beyond this point, partial IAR cannot be achieved in any case. Overall, the float-to-fixed RMS ratios in all three directions decrease as the cut-off elevation rises from 5° and higher for the Iridium-only case.

Previous results suggest that one cannot achieve reliable and efficient partial IAR if the cut-off elevation exceeds 20° for the Iridium-only case. We then consider a more extreme scenario with a higher cut-off, e.g., above 50°, where multi-LEO/GNSS constellations are included to enable positioning. For a sampling interval Δt of 1 s as shown in the left sub-figure in Fig. 15, fixing ambiguities is feasible for the stations with more than multi-LEO/GNSS 15 satellites, resulting in approximately 73%, 55% and 65% improvements in the north, east and up directions, respectively, for all stations successfully achieving partial IAR. Notably, by applying partial IAR, the ALBH and BJNM stations exhibit improvements in the RMSs of the positioning errors close to 100% in all three directions, achieving millimeter-level positioning accuracy. At the ALRT station however, the minimum success-rate requirement (99%) is not reached, limiting the position solutions to centimeter-level accuracy. This is because this station tracks a relatively low proportion of Starlink satellites among all LEO satellites (2 out of 13). Other stations also exhibit a similar trend: given a sufficient number of available multi-LEO/GNSS satellites, a higher proportion of Starlink satellites is associated with an increased likelihood of successfully fixing ambiguities. Starlink, with the lowest altitude of approximately 550 km among the constellations we used, shows the most rapid geometric changes compared to the remaining constellations. This characteristic is advantageous for obtaining more precise float ambiguities and achieving ambiguity resolution, particularly for short sampling intervals (e.g., 1 s).

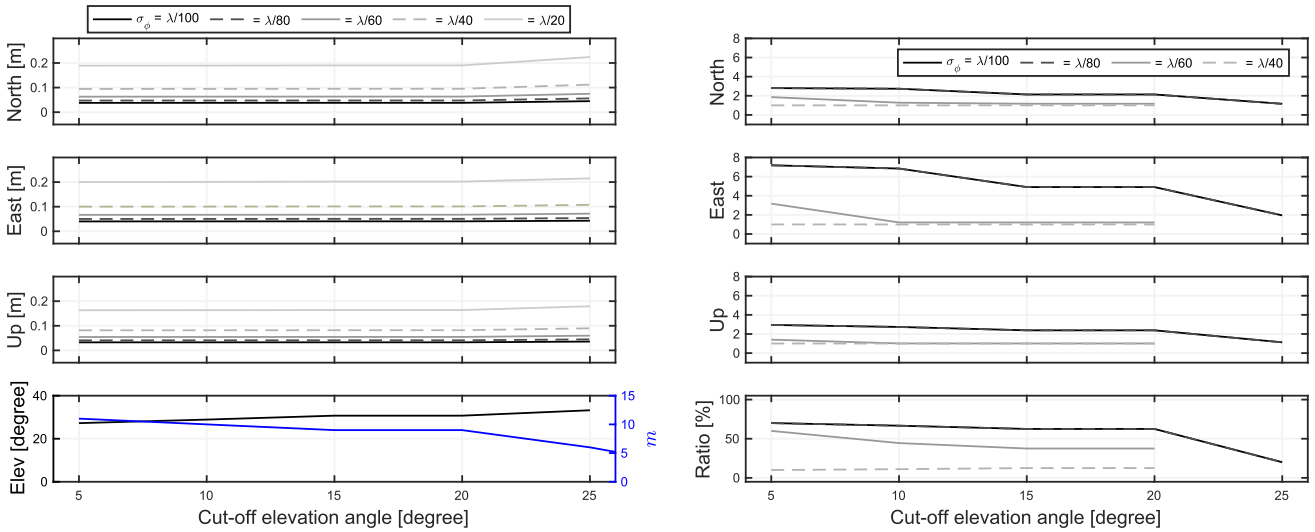

Fig. 14 RMSs (m) of ambiguity-float positioning solutions (left) and the corresponding float-to-fixed RMS ratios and fixed-to-all ambiguity number ratios after partial IAR with a minimum required ILS success-rate of 99.9% (right) as a function of the cut-off elevation for different carrier phase measurement precision σ_ϕ, based on the dual-epoch phase-only model (14) with a 30-s sampling interval Δt for the 5-km baseline located in station NYAL, observing Iridium satellites. For simplicity, only the simulation results at 5400 s on December 19, 2023 are presented. Note, for $\sigma_\phi = 1/20$ cycles, the minimum success-rate requirement is not met. Thus, the corresponding fixed results are absent

Benefiting from the longer sampling interval, e.g., Δt = 30 s as shown in the right sub-figure in Fig. 15, all stations except DGAR achieve ambiguity-float positioning errors of less than 10 cm in all three directions. The DGAR station is excluded because it delivers a 3-dimensional ambiguity-float positioning accuracy at the meter level and cannot meet the minimum required success rate for partial IAR, due to the presence of only 2 LEO and 5 GNSS satellites. Compared to a 1-s sampling interval, a 30-s sampling interval yields fewer co-visible LEO satellites over two epochs due to the rapid motion of LEO satellites. By applying partial IAR, the remaining 13 stations show average improvements of approximately 48%, 69% and 37% in the north, east and up directions, respectively, with the most significant improvement observed in the east component. These stations ultimately achieve millimeter-level horizontal and centimeter-level vertical accuracy using multi-LEO/GNSS satellites.

To conclude this section, we summarize all results of the performance of the dual-epoch phase-only positioning for combined LEO and GNSS constellations in Table 3.

6 Summary and conclusions

In this contribution, we explored the performance of ambiguity-resolved LEO short-baseline positioning using frequency-varying carrier phase signals under the dual-epoch phase-only model (14). In the absence of code measurements, it was shown that certain condition must hold in order to discard the measurement bias that is generated when evaluating satellite clock and orbital corrections at the signal transmission time. While single-receiver high-precision LEO-based positioning can be challenging, we leveraged the relative distance between a base and rover receivers, identifying the conditions under which short-baseline positioning can potentially overcome inaccuracies in the LEO satellite orbit and clock products. Accordingly, the baseline is assumed to be sufficiently short (e.g., 5 km), while the receivers are assumed to be equipped with high-grade clocks, ensuring that the SD clock offset remains below 0.1 microseconds. These assumptions, along with access to decimeter-level orbit products, were made to guarantee that the stated bias is smaller than the millimeter-level noise of the carrier phase measurements. With the single-epoch phase-and-code model as reference, key performance metrics were derived to provide an initial insight into the capability of standalone LEO-based phase-only positioning. LEO constellations were shown to have its own distinct response to IAR. Therefore, we carried out a simulation study to assess the ambiguity-resolved positioning performance of standalone and combined LEO/GNSS constellations. Our main findings are summarized as follows:

- If Iridium and OneWeb satellites broadcast phase measurements as precise as those of GNSS, i.e., $\sigma_\phi = 1/100$ cycles, the dual-epoch phase-only model, with a 1-s sampling-rate, is capable of delivering meter- and decimeter-levels float positioning solutions, respectively. However, while successful full IAR is advantageous for positioning, it appears to be infeasible for this model.

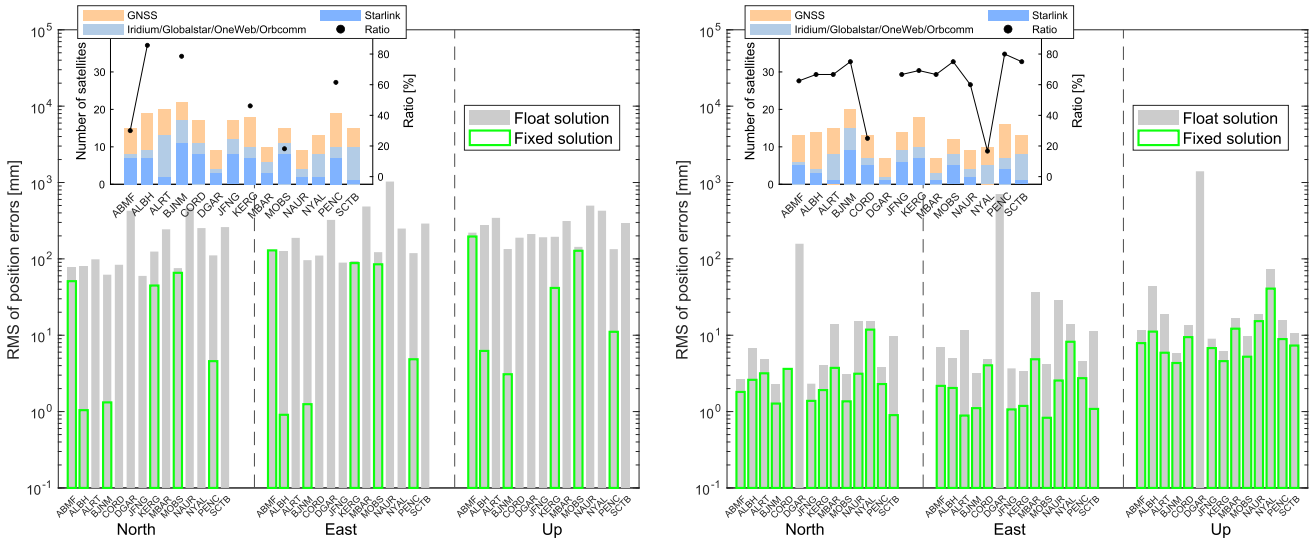

Fig. 15 RMSs (mm) of ambiguity-float positioning errors (gray bar charts) and their fixed versions (green boxes) after partial IAR with a minimum required ILS success-rate of 99.9%, based on the dual-epoch phase-only model (14) at a cut-off elevation angle of 50° for 14 IGS stations, where the carrier phase measurement precision is 1/40 cycles. The top-left inset in each figure illustrates the available satellite numbers of each constellation (vertical bar charts with different colors) and the fixed-to-all ambiguity number ratios (black lines) for the 14 stations. The left and right subfigures are the results of 1-s and 30-s sampling intervals, respectively. GNSS includes frequency-identical GPS/Galileo and frequency-varying GLONASS signals, while LEO includes frequency-varying Iridium/Globalstar/Starlink/OneWeb/Orbcomm signals. For simplicity, only the simulation results at 5400 s on December 19, 2023 are presented

- One therefore has to consider partial IAR instead. For the Iridium constellation, although the partial ADOP is almost 4 times smaller than its full version in some cases, it does not result in a significant precision gain in the positioning results. The results also indicate that the reduction in partial ADOP compared to that of full IAR may not be considerable for the OneWeb case.
- The empirical analysis verifies, if the SD clock offset is less than 0.1 microseconds, that there is no considerable effect on the partial-fixed positioning solutions. The capability for ambiguity-float positioning enhances as the number of LEO satellites increases. However, partial IAR is not achieved even with the maximum currently available 11 Iridium satellites, based on the dual-epoch phase-only model with a 1-s sampling interval. By contrast, with a sufficient number of satellites (up to 34), as well as greater differences in frequency ratios, the OneWeb constellation can achieve 3-dimensional millimeter-level positioning accuracy with a 1-s sampling interval when the phase measurement precision is set to 1/100 cycles.
- The limited number of standalone Iridium and Globalstar satellites broadcasting L-band signals, as observed by stations in mid- to low-latitude regions, prevents them from achieving partial IAR. Being augmented with GNSS however, these two LEO constellations can deliver millimeter-level positioning solutions when more than 25 satellites are available, specifically in the case of 1-s sampling interval and a phase measurement precision of 1/80 cycles.
- One cannot achieve cm-level positioning if the cut-off elevation exceeds 20° in the standalone Iridium case. To ensure a sufficient number of satellites in high-cut-off GNSS(and/or LEO)-challenged environments, such as at a cut-off of 50°, the five LEO constellations (Table 1) are combined with three GNSS constellations (GPS, GLONASS, and Galileo), showing that partial IAR is feasible for the stations observing more than 15 satellites, resulting in a precision improvement of over 50% in all three directions for the near-real-time (1-s interval) positioning solutions when the phase measurement precision is 1/40 cycles. By extending the sampling interval from 1 s to 30 s, 13 out of 14 globally distributed short baselines show average improvements of approximately 48%, 69% and 37% in the north, east and up directions, respectively, ultimately achieving millimeter-level horizontal and centimeter-level vertical partial-fixed precision.

Table 3 RMSs of positioning errors for 14 globally distributed short baselines (~ 5 km) using various combinations of multi-LEO/GNSS constellations corresponding to the dual-epoch phase-only model (14). The fixed solutions correspond to partial IAR with a minimum required ILS success-rate of 99.9%. The 'ratio1' represents the number of stations obtaining ambiguity-float solutions relative to the total number of stations, while the 'ratio2' denotes the number of stations successfully achieving partial IAR relative to the number of stations obtaining ambiguity-float solutions. GNSS includes frequency-identical GPS/Galileo and frequency-varying GLONASS signals, while LEO includes frequency-varying Iridium/Globalstar/Starlink/OneWeb/Orbcomm signals. For simplicity, only the simulation results at 5400 s on December 19, 2023 are presented

	Cut-off [degrees]	m	σ_ϕ [cycles]	Δt [s]	Ratio1	RMS of $\hat{x}$ [cm]	Ratio2	RMS of $\check{x}$ [cm]
Iridium/ Globalstar	5	2–12	1/80	30	11/14	N: 2.4–81.9 E: 2.5–633.8 U: 3.4–291.8	2/11	N: 0.9–1.7 E: 0.7–1.9 U: 1.4–1.8
GNSS/Iridium/ Globalstar	5	25–42	1/80	30	14/14	N: 1.9–43.9 E: 1.9–98.7 U: 3.4–37.4	14/14	N: 0.1–0.2 E: 0.1–0.2 U: 0.3–0.5
GNSS/LEO	50	7–20	1/60	30	14/14	N: 0.2–15.8 E: 0.2–70.6 U: 0.4–140.3	13/14	N: 0.1–1.1 E: 0.1–0.6 U: 0.3–3.2
GNSS/LEO	50	7–20	1/40	30	14/14	N: 0.2–15.8 E: 0.3–70.6 U: 0.6–140.3	13/14	N: 0.1–1.2 E: 0.1–0.8 U: 0.4–4.1
GNSS/LEO	50	7–20	1/20	30	14/14	N: 0.5–15.8 E: 0.6–70.6 U: 1.1–140.3	13/14	N: 0.3–1.4 E: 0.2–1.3 U: 0.8–6.5
GNSS/LEO	50	9–22	1/60	1	14/14	N: 4.0–39.7 E: 6.0–89.5 U: 8.9–34.2	9/14	N: 0.1–6.0 E: 0.0–11.0 U: 0.2–19.8
GNSS/LEO	50	9–22	1/40	1	14/14	N: 6.0–46.5 E: 8.9–102.9 U: 13.4–49.8	6/14	N: 0.1–6.6 E: 0.1–12.9 U: 0.3–19.6
GNSS/LEO	50	9–22	1/20	1	14/14	N: 11.9–62.6 E: 15.8–130.2 U: 26.8–96.7	3/14	N: 0.5–15.3 E: 0.6–25.3 U: 1.3–45.1

Future research will focus on Kalman filter-based kinematic positioning, as well as the integration of LEO satellites with different navigation satellite systems to evaluate the resultant ambiguity-resolved positioning performance.

Appendix A: Supplementary proofs

Proof of (6) Let $\dot{x}^s$ and g_r^s, respectively, be the satellite velocity vector and the satellite-to-receiver LOS direction vector corresponding to satellite s and receiver r. The first part I follows from the definition of the bias entry ε_t^s, while the remaining decomposition (6) follows by the first-order Taylor series expansion of function $\bar{\phi}_t^s(x_r^\circ, t_b^s, t_r^s, \tau_b^s, \tau_r^s)$ in (2) about the point $(x_r^\circ, \hat{t}_b^s, \hat{t}_r^s, \hat{\tau}_b^s, \hat{\tau}_r^s)$, and recognizing the partial derivatives of $||x_r^\circ - x^s(t)||$ with respect to x^s as $-g_r^s$, and with respect to t as $-v_r^s$, with $v_r^s = g_r^s\, \dot{x}^s$ being the LOS velocity. □

Proof of Lemma (1) Application of the minimum variance least-squares estimation to the PC model (11) gives the variance matrices of the float and fixed position solutions $\hat{x}$ and $\check{x}$, respectively, as follows (Teunissen 1997)

$$\begin{aligned} Q_{\hat{x}\hat{x}} &= 2\sigma_p^2 \left(G_t W_t P G_t \right)^{-1} \\ Q_{\check{x}\check{x}} &= \left(Q_{\hat{x}\hat{x}}^{-1} + \tfrac{1}{2\lambda^2\sigma_\phi^2} \left(G_t \bar{W}_t \bar{P} G_t \right) \right)^{-1} \end{aligned} \tag{30}$$

Taking the determinant of the first equation in (30) gives $|Q_{\hat{x}\hat{x}}| = (2\sigma_p^2)^3 / |G_t W_t P G_t|$, from which the first expression of (24) follows. Pre-multiplying the inverse of the second equation with the first in (30) gives

$$Q_{\hat{x}\hat{x}} Q_{\check{x}\check{x}}^{-1} = I_3 + \frac{\sigma_p^2}{\lambda^2\sigma_\phi^2} (G_t W_t P G_t)^{-1} (G_t \bar{W}_t \bar{P} G_t) \tag{31}$$

From the determinant of the above equation follows that

$$\mathcal{G}_{\hat{x}} = \iota \frac{\sigma_p}{\lambda\, \sigma_\phi} \, |I_3 + \epsilon\, (G_t \bar{W}_t \bar{P} G_t)^{-1} (G_t W_t P G_t)|^{\frac{1}{6}} \tag{32}$$

where $\epsilon = (\lambda^2\sigma_\phi^2)/\sigma_p^2$. The second expression of (24) is an approximation of (32) when $\epsilon \approx 0$, i.e., when the phase data are assumed to be much more precise than their code counterparts. The last expression, i.e., the ADOP expression, follows from the results in (Teunissen 2019, pp. 11). □

Proof of Lemma (2) Since the minimum variance least-squares solutions remain invariant for a one-to-one linear transformation of the observations, one can instead of the P model (14), equivalently work with the following model

$$\tfrac{1}{2}\mathsf{E}\left(\begin{bmatrix} \Delta\phi_{t+1} + \Delta\phi_t \\ \Delta\phi_{t+1} - \Delta\phi_t \end{bmatrix} \right) = \begin{bmatrix} G \\ \frac{1}{2}\dot{G}\, \Delta t \end{bmatrix} \Delta x + \tfrac{1}{2} \begin{bmatrix} e \\ e \end{bmatrix} d\tilde{t}_{t+1}$$

$$+\tfrac{1}{2}\begin{bmatrix}\Lambda\\0\end{bmatrix}\tilde{a} \tag{33}$$

Compare the above model with the single-epoch PC model (11). Apart from the design matrix $(1/2)\dot{G}\,\Delta t$ replacing G_t, the model (33) is identical in structure to (11). Making the approximation $W_{t+1} \approx W_t \approx W$, the epoch-differenced data $(\Delta\phi_{t+1} - \Delta\phi_t)$ is uncorrelated with the epoch-averaged data $(\Delta\phi_{t+1} + \Delta\phi_t)/2$ (Khodabandeh and Teunissen 2018). Along the same lines as the proof of Lemma (1), the expressions in (26) can therefore be derived. □

Proof of Lemma (3) To prove the first expression of (28), we use the identity $\mathcal{G}^{\mathrm{PAR}}_{\hat{x}}/\mathcal{G}^{\mathrm{FAR}}_{\hat{x}} = 1/|Q^{\mathrm{PAR}}_{\check{x}\check{x}}\,Q^{-1}_{\check{x}\check{x}}|^{\frac{1}{6}}$ in which the variance matrix of the partially ambiguity-fixed position solution reads

$$Q^{\mathrm{PAR}}_{\check{x}\check{x}} = Q_{\check{x}\check{x}} + \frac{1}{l^T Q^{-1}_{\hat{z}\hat{z}}\, l}\, Q_{\hat{x}\hat{z}} Q^{-1}_{\hat{z}\hat{z}}\, l\, l^T\, Q^{-1}_{\hat{z}\hat{z}}\, Q_{\hat{z}\hat{x}} \tag{34}$$

The expression follows then by post-multiplying (34) with $Q^{-1}_{\check{x}\check{x}}$ and using the determinant identity (Koch 1999)

$$\begin{aligned}&|I_3 + \tfrac{1}{l^T Q^{-1}_{\hat{z}\hat{z}}\, l}\, Q_{\hat{x}\hat{z}} Q^{-1}_{\hat{z}\hat{z}}\, l\, l^T\, Q^{-1}_{\hat{z}\hat{z}}\, Q_{\hat{z}\hat{x}}\, Q^{-1}_{\check{x}\check{x}}|\\ &\quad = |1 + \frac{l^T Q^{-1}_{\hat{z}\hat{z}}\, Q_{\hat{z}\hat{x}} Q^{-1}_{\check{x}\check{x}} Q_{\hat{x}\hat{z}} Q^{-1}_{\hat{z}\hat{z}}\, l}{l^T Q^{-1}_{\hat{z}\hat{z}}\, l}|\end{aligned} \tag{35}$$

To provide the second expression of (28), we make use of the property that the determinant of the admissible ambiguity matrix $[\tilde{L}, \tilde{l}]$ is ± 1, and thus $|Q_{\hat{z}\hat{z}}| = |[\tilde{L}, \tilde{l}]^T Q_{\hat{z}\hat{z}} [\tilde{L}, \tilde{l}]|$. With the aid of the determinant identity (Koch 1999)

$$\begin{vmatrix}\tilde{L}^T Q_{\hat{z}\hat{z}}\tilde{L} & \tilde{L}^T Q_{\hat{z}\hat{z}}\tilde{l}\\ \tilde{l}^T Q_{\hat{z}\hat{z}}\tilde{L} & \tilde{l}^T Q_{\hat{z}\hat{z}}\tilde{l}\end{vmatrix} = \frac{|\tilde{L}^T Q_{\hat{z}\hat{z}}\tilde{L}|}{|l^T Q^{-1}_{\hat{z}\hat{z}}\, l|}, \tag{36}$$

and $Q_{\hat{z}_1\hat{z}_1} = \tilde{L}^T Q_{\hat{z}\hat{z}}\tilde{L}$, we get $|Q_{\hat{z}_1\hat{z}_1}| = |Q_{\hat{z}\hat{z}}|\,|l^T Q^{-1}_{\hat{z}\hat{z}}\, l|$, from which the second expression of (28) follows. □

Appendix B: Impact of orbital biases

The presence of the bias vector ε_t in (4) is due to the error in estimating the signal transmission time vectors $t_r - \tau_r$ and $t_b - \tau_b$. By considering sufficiently short baselines and having receivers equipped with high-grade clocks, the stated bias vector can be discarded, i.e., $\varepsilon_t \approx 0$. This, however, relies on a crucial assumption of having precise satellite orbit products. As (2) indicates, the computed measurement vector $\bar{\phi}^s_t$ depends on the satellite position vectors are given by x^s $(s = 1, \ldots, m)$. If each of these vectors are biased as $x^s \mapsto x^s + \beta^s$, the observation equations (4) read $(\varepsilon_t \approx 0)$

$$\mathsf{E}(\Delta\phi_t) = G_t\,\Delta x + e\,dt_t + \Lambda\,a + \Delta\rho \tag{37}$$

with the between-receiver SD range bias vector $\Delta\rho = [\Delta\rho^s_r - \Delta\rho^s_b]$, where $\Delta\rho^s_r = ||x^\circ_r - (x^s + \beta^s)|| - ||x^\circ_r - x^s||$. Figure 16 (left-panel) compares the entries of $\Delta\rho_t$ of the GPS satellites (top) with those of the Iridium and OneWeb satellites (bottom). The baseline is set to be 5 km. The results are generated using the 3×1 orbital bias vectors $\beta^s = (1/\sqrt{3})[5, 5, 5]^T$ meters. Thus, the norm of the orbital bias vectors is set to $||\beta^s|| = 5$ meters. Thanks to the rather high altitude of the GPS satellites, these orbital biases deliver SD range biases smaller than 0.8 mm (top-left). However, the results corresponding to the Iridium and OneWeb LEO satellites can reach 12 mm (bottom-left).

Note that only part of the SD range bias vector $\Delta\rho$ will affect the fixed position solution $\check{x}$. To identify this part, assume that the integer-estimable ambiguities $z = F^T a$ are correctly resolved. The design matrix of (37) would then read $[G_t, e]$. This is because the inestimable part of a is absorbed by the receiver clock dt_t. To eliminate the presence of dt_t, the design matrix of Δx, G_t is reduced to $A_t = \bar{P}G_t$, where the projector $\bar{P}$ forms between-satellite differences, i.e., $\bar{P}e = 0$. Application of least-squares estimation gives $A^+_t\Delta\rho = (G_t\bar{W}_t\bar{P}G_t)^{-1}G_t\bar{W}_t\bar{P}\Delta\rho$, with A^+_t being the least-squares inverse of A_t. The component $A^+_t\Delta\rho$ is absorbed by the fixed solution $\check{x}$. To show the contribution of each satellite to this component, in Fig. 16 (right-panel) we evaluate its projection on the observation equations (37), i.e., $A_tA^+_t\Delta\rho$. As shown, the orbital component affecting $\check{x}$ for GPS is smaller than 0.6 mm, while this component for Iridium/OneWeb is less than 6 mm. By decreasing the magnitude of the orbital bias vector β^s, we have observed that the SD range bias vector $\Delta\rho$ almost linearly decreases. For instance, the decimeter-level bias $||\beta^s|| = 50$ cm leads to an SD range bias vector with $||\Delta\rho|| \leq 1.2$ mm whose component $A^+_t\Delta\rho$ is less than 0.6 mm. To ensure that the magnitude of the SD range bias vector remains below mm-level, the orbital bias should be maintained at the decimeter level.

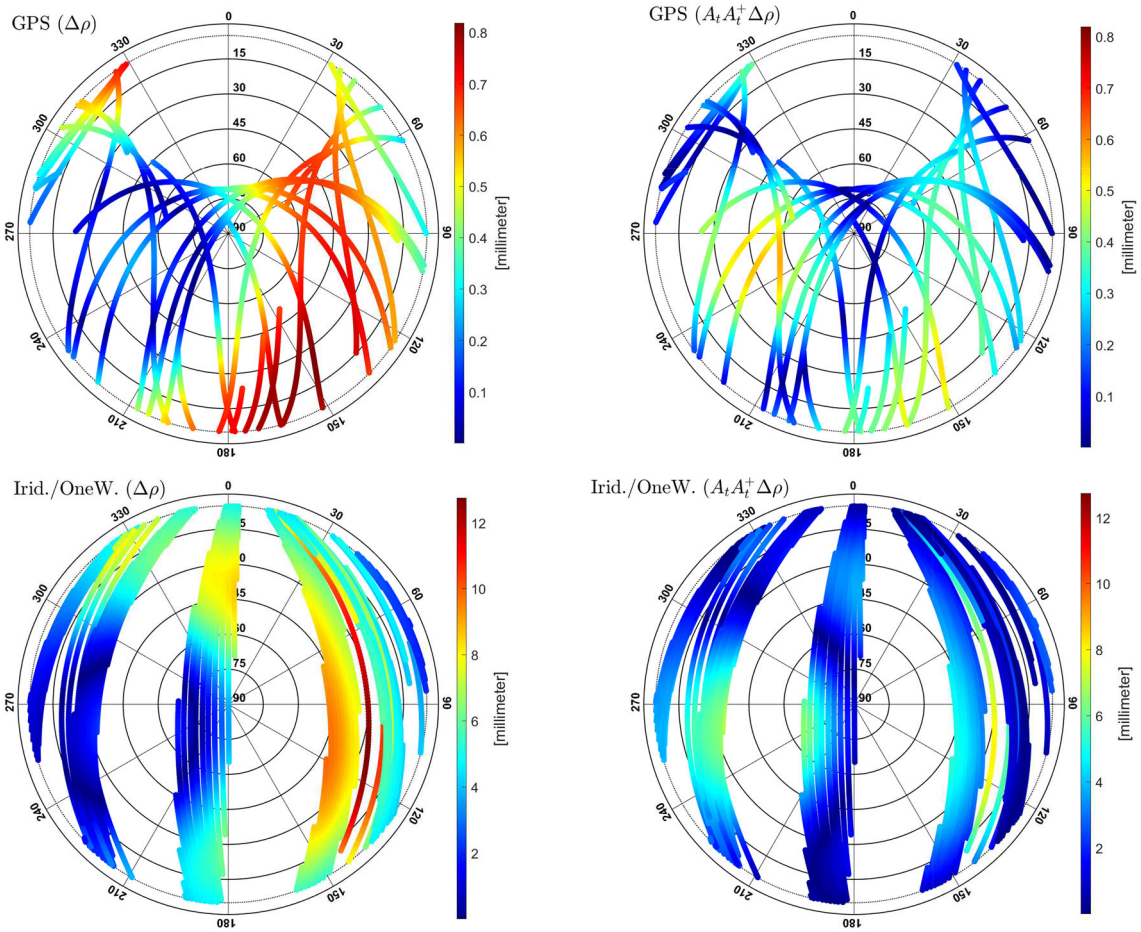

Fig. 16 Absolute values of the entries of the between-receiver SD bias vector $\Delta\rho = [\Delta\rho_r^s - \Delta\rho_b^s]$ (left) in (37) and those of its projection $A_t A_t^+ \Delta\rho$ (right) corresponding to the orbital biases $\beta^s = (1/\sqrt{3})[5, 5, 5]^T$ [m], for the BJNM (located in China) short-baseline observing GPS (top) and Iridium/OneWeb satellites (bottom) on the day of year 353, 2023. The baseline is set to be 5 km. Each line in the skyplot corresponds to a satellite path

Acknowledgements We thank the reviewers for their constructive feedback and valuable suggestions. The provision of LEO and GNSS data by CelesTrak and the International GNSS Service (IGS) is gratefully acknowledged. Support from the University of Melbourne's Research Computing Services and the Petascale Campus Initiative is also appreciated. The first author expresses gratitude for the financial support received from the University of Melbourne through the Melbourne Research Scholarship.

Author Contributions SY and AK developed the concept and wrote the manuscript. SY processed the data and provided the numerical results. SZ and PJGT reviewed and edited the manuscript.

Data availability The data used in this contribution are available at the following URL: https://cddis.nasa.gov/archive/gnss/products/ for GNSS orbit products and https://celestrak.org/NORAD/elements/ for LEO TLE files.

Declarations

Conflict of interest The authors have no conflict of interest that are relevant to the content of this paper.

References

Allahvirdi-Zadeh A, Wang K, El-Mowafy A (2022) Precise orbit determination of LEO satellites based on undifferenced GNSS observations. J Survey Eng 148(1):03121001

Bloch M, Ho J, Mancini O, McClelland T (2012) Iridium-NEXT master clock. In: 2012 European frequency and time forum, IEEE, pp 260–262

Brack A (2017) Reliable GPS+ BDS RTK positioning with partial ambiguity resolution. GPS Solut 21(3):1083–1092

Brack A, Männel B, Schuh H (2021) GLONASS FDMA data for RTK positioning: a five-system analysis. GPS Solut 25(1):1–13

de Jonge PJ (1998) A processing strategy for the application of the GPS in networks. PhD thesis, Delft University of Technology, Publication on Geodesy, 46, Netherlands Geodetic Commission, Delft

Dietrich FJ, Metzen P, Monte P (1998) The globalstar cellular satellite system. IEEE Trans Antennas Propag 46(6):935–942

Fang J, Tu R, Zhang P, Zhang R, Lu X (2024) UPDs estimation and ambiguity resolution performance evaluation of LEO navigation system. Advances in space research

Ge H, Li B, Jia S, Nie L, Wu T, Yang Z, Shang J, Zheng Y, Ge M (2022) LEO enhanced global navigation satellite system (LeGNSS): Progress, opportunities, and challenges. Geo-spatial Inf Sci 25(1):1–13

Hayek S, Saroufim J, Neinavaie M, Kozhaya S, Kassas ZM (2023) Assessment of differential Doppler navigation with Starlink LEO satellite signals of opportunity. In: Proceedings of the 2023 international technical meeting of The institute of navigation, pp 1021–1031

Hou P, Zhang B, Liu T (2020) Integer-estimable GLONASS FDMA model as applied to Kalman-filter-based short-to long-baseline RTK positioning. GPS Solut 24(4):93

Hou P, Zhang B, Yasyukevich YV, Liu T, Zha J (2022) Multi-frequency phase-only PPP-RTK model applied to BeiDou data. GPS Solut 26(3):76

Huisman L, Teunissen PJ, Odijk D (2010) On the robustness of next generation GNSS phase-only real-time kinematic positioning. In: Proc. of FIG Congress, Sydney, Australia

Humphreys TE, Iannucci PA, Komodromos ZM, Graff AM (2023) Signal structure of the Starlink Ku-band downlink. IEEE Trans Aerosp Electron Syst 59(5):6016–6030

Ilcev SD (2005) Global mobile satellite communications: For maritime, land and aeronautical applications. Springer Science and Business Media

Kassas Z, Khalife J, Neinavaie M (2024) Navigation with differential carrier phase measurement from low earth orbit satellites. US Patent 11,953,607

Kassas Z, Neinavaie M, Khalife J, Khairallah N, Kozhaya S, Haidar-Ahmad J, Shadram Z (2021) Enter LEO on the GNSS stage: Navigation with Starlink satellites. Inside GNSS

Khairallah N, Kassas ZM (2022) An interacting multiple model estimator of LEO satellite clocks for improved positioning. In: 2022 IEEE 95th vehicular technology conference:(VTC2022-Spring), IEEE, pp 1–5

Khalife J, Kassas ZZM (2023) Performance-driven design of carrier phase differential navigation frameworks with megaconstellation LEO satellites. IEEE Trans Aerosp Electron Syst 59(3):2947–2966

Khalife J, Kassas ZM (2019) Receiver design for Doppler positioning with LEO satellites. In: ICASSP 2019 - 2019 IEEE International conference on acoustics, speech and signal processing (ICASSP), pp 5506–5510, 10.1109/ICASSP.2019.8682554

Khodabandeh A, Teunissen PJG (2018) On the impact of GNSS ambiguity resolution: geometry, ionosphere, time and biases. J Geod 92(6):637–658

Khodabandeh A, Zaminpardaz S, Nadarajah N (2021) A study on multi-GNSS phase-only positioning. Measurement Sci Technol 32(9):095005

Khodabandeh A, Teunissen PJG (2023) Ambiguity-fixing in frequency-varying carrier phase measurements: Global navigation satellite system and terrestrial examples. NAVIGATION: J Inst Navig 70(2), 10.33012/navi.580

Koch KR (1999) Parameter estimation and hypothesis testing in linear models. Springer, Berlin

Kozhaya S, Kanj H, Kassas ZM (2023) Multi-constellation blind beacon estimation, Doppler tracking, and opportunistic positioning with OneWeb, Starlink, Iridium NEXT, and Orbcomm LEO satellites. 2023 IEEE/ION Position. IEEE, Location and Navigation Symposium (PLANS), pp 1184–1195

Leick A, Rapoport L, Tatarnikov D (2015) GPS satellite surveying, 4th edn. Wiley, New York

Li X, Li X, Ma F, Yuan Y, Zhang K, Zhou F, Zhang X (2019) Improved PPP ambiguity resolution with the assistance of multiple LEO constellations and signals. Remote Sensing 11(4):408

Li W, Yang Q, Du X, Li M, Zhao Q, Yang L, Qin Y, Chang C, Wang Y, Qin G (2024) LEO augmented precise point positioning using real observations from two CENTISPACE™ experimental satellites. GPS Solut 28(1):44

Odijk D (2017) Positioning model. In: Teunissen PJG, Montenbruck O (eds) Springer handbook of global navigation satellite systems, Springer, chap 21, pp 605–638

Odijk D, Teunissen PJG (2008) ADOP in closed form for a hierarchy of multi-frequency single-baseline GNSS models. J Geod 82(8):473–492

Odolinski R, Teunissen PJG, Odijk D (2015) Combined BDS, Galileo, QZSS and GPS single-frequency RTK. GPS Solut 19(1):151–163

Orabi M, Khalife J, Kassas ZM (2021) Opportunistic navigation with Doppler measurements from Iridium Next and Orbcomm LEO Satellites. In: 2021 IEEE Aerospace conference (50100), pp 1–9, 10.1109/AERO50100.2021.9438454

Psychas D, Verhagen S, Teunissen PJG (2020) Precision analysis of partial ambiguity resolution-enabled PPP using multi-GNSS and multi-frequency signals. Adv Space Res 66(9):2075–2093

Reid TGR, Neish AM, Walter T, Enge PK (2018) Broadband LEO constellations for navigation. NAVIGATION: J Inst Navig 65(2):205–220

Reid T, Banville S, Chan B, Gunning K, Manning B, Marathe T, Neish A, Perkins A, Sibois A (2022) PULSAR: a new generation of commercial satellite navigation. ION GNSS+ 2022 pp 11–15

Rybak MM, Axelrad P, Seubert J, Ely T (2021) Chip scale atomic clock-driven one-way radiometric tracking for low-earth-orbit Cubesat navigation. J Spacecr Rockets 58(1):200–209

Saroufim J, Hayek SW, Kassas ZM (2023) Simultaneous LEO satellite tracking and differential LEO-aided IMU navigation. 2023 IEEE/ION position. IEEE, Location and Navigation Symposium (PLANS), pp 179–188

Shi C, Zhang Y, Li Z (2023) Revisiting Doppler positioning performance with LEO satellites. GPS Solut 27(3):126

Teunissen PJG (2019) A new GLONASS FDMA model. GPS Solut 23(100)

Teunissen PJG, Joosten P, Tiberius CCJM (1999) Geometry-free ambiguity success rates in case of partial fixing. In: Proceedings of the 1999 national technical meeting of the institute of navigation, pp 201–207

Teunissen PJG, Montenbruck O (eds) (2017) Springer handbook of global navigation satellite systems. Springer

Teunissen PJG (1995) The least-squares ambiguity decorrelation adjustment: a method for fast GPS integer ambiguity estimation. J Geod 70(1–2):65–82

Teunissen PJG (1997) A canonical theory for short GPS baselines. Part I: The baseline precision. J Geod 71(6):320–336

Teunissen PJG (1999) An optimality property of the integer least-squares estimator. J Geod 73(11):587–593

Teunissen PJG, Khodabandeh A (2019) GLONASS ambiguity resolution. GPS Solut 23:101. https://doi.org/10.1007/s10291-019-0890-7

Teunissen PJG, Khodabandeh A (2022) PPP-RTK theory for varying transmitter frequencies with satellite and terrestrial positioning applications. J Geod 96(11):84

Vallado D, Crawford P (2008) SGP4 orbit determination. In: AIAA/AAS Astrodynamics specialist conference and exhibit, p 6770

Verhagen S, Li B, Teunissen PJG (2013) Ps-LAMBDA: ambiguity success rate evaluation software for interferometric applications. Comput Geosci 54:361–376

Wang K, Chen P, Teunissen PJG (2018) Fast phase-only positioning with triple-frequency GPS. Sensors 18(11):3922. https://doi.org/10.3390/s18113922

Wang L, Chen R, Li D, Zhang G, Shen X, Yu B, Wu C, Xie S, Zhang P, Li M et al (2018) Initial assessment of the LEO based navigation signal augmentation system from Luojia-1A satellite. Sensors 18(11):3919

Wang K, El-Mowafy A, Sun B, Yang X (2024) LEO augmentation in wide-area PPP-RTK positioning and time transfer. In: International GNSS service (IGS) symposium

Xu S, Yang Q, Du X, Xu X, Zhao Q, Yang L, Qin Y, Guo J (2024) Multi-GNSS precise point positioning enhanced by the real navigation signals from CENTISPACE™ LEO mission. Adv Space Res 73(8):4175–4186

Yang Y, Mao Y, Ren X, Jia X, Sun B (2024) Demand and key technology for a LEO constellation as augmentation of satellite navigation systems. Satell Navig 5(1):11

Zaminpardaz S, Teunissen PJG, Khodabandeh A (2021) GLONASS-only FDMA+ CDMA RTK: performance and outlook. GPS Solut 25(3):96

Zhang B, Hou P, Zha J, Liu T (2021) Integer-estimable FDMA model as an enabler of GLONASS PPP-RTK. J Geod 95:1–21

Zhang Y, Qin H, Shi G (2023) Doppler positioning based on Globalstar signals of opportunity. In: 2023 5th International conference on electronic engineering and informatics (EEI), IEEE, pp 666–669